

MICROLENSING OPTICAL DEPTH TOWARD THE GALACTIC BULGE FROM MICROLENSING OBSERVATIONS IN ASTROPHYSICS GROUP OBSERVATIONS DURING 2000 WITH DIFFERENCE IMAGE ANALYSIS

T. SUMI,^{1,2} F. ABE,² I. A. BOND,³ R. J. DODD,^{4,5} J. B. HEARNshaw,⁶ M. HONDA,⁷ M. HONMA,⁸ Y. KAN-YA,⁸ P. M. KILMARTIN,⁶ K. MASUDA,² Y. MATSUBARA,² Y. MURAKI,² T. NAKAMURA,⁹ R. NISHI,¹⁰ S. NODA,⁸ K. OHNISHI,¹¹ O. K. L. PETTERSON,⁶ N. J. RATTENBURY,¹² M. REID,⁵ TO. SAITO,¹³ Y. SAITO,² H. SATO,¹⁴ M. SEKIGUCHI,⁷ J. SKULJAN,⁶ D. J. SULLIVAN,⁵ M. TAKEUTI,¹⁵ P. J. TRISTRAM,⁶ S. WILKINSON,⁵ T. YANAGISAWA,¹⁶ AND P. C. M. YOCK¹²

Received 2002 July 27; accepted 2003 February 27

ABSTRACT

We analyze the data of the gravitational microlensing survey carried out by the Microlensing Observations in Astrophysics (MOA) group during 2000 toward the Galactic bulge (GB). Our observations are designed to detect efficient high-magnification events with faint source stars and short-timescale events, by increasing the sampling rate up to ~ 6 times per night and using Difference Image Analysis (DIA). We detect 28 microlensing candidates in 12 GB fields corresponding to 16 deg^2 . We use Monte Carlo simulations to estimate our microlensing event detection efficiency, where we construct the *I*-band extinction map of our GB fields in order to find dereddened magnitudes. We find a systematic bias and large uncertainty in the measured value of the timescale $t_{E,\text{out}}$ in our simulations. They are associated with blending and unresolved sources, and are allowed for in our measurements. We compute an optical depth $\tau = 2.59^{+0.84}_{-0.64} \times 10^{-6}$ toward the GB for events with timescales $0.3 < t_E < 200$ days. We consider disk-disk lensing, and obtain an optical depth $\tau_{\text{bulge}} = 3.36^{+1.11}_{-0.81} \times 10^{-6} [0.77 / (1 - f_{\text{disk}})]$ for the bulge component assuming a 23% stellar contribution from disk stars. These observed optical depths are consistent with previous measurements by the MACHO and OGLE groups, and still higher than those predicted by existing Galactic models. We present the timescale distribution of the observed events, and find there are no significant short events of a few days, in spite of our high detection efficiency for short-timescale events down to $t_E \sim 0.3$ days. We find that half of all our detected events have high magnification (> 10). These events are useful for studies of extrasolar planets.

Subject headings: dark matter — Galaxy: halo — gravitational lensing

1. INTRODUCTION

Following the suggestion of Paczyński (1991) and Griest et al. (1991), several groups have carried out microlensing surveys toward the Galactic bulge (GB), as seen in Baade's window. It is now well understood that these observations are useful for studying the structure, dynamics, and kinematics of the Galaxy and the stellar mass function, as the event rate and timescale distributions are related to the masses and velocities of lens objects.

The amplification of a microlensing event is described by (Paczynski 1986)

$$A(u) = \frac{u^2 + 2}{u\sqrt{u^2 + 4}}, \quad (1)$$

where u is the projected separation of the source and lens in units of the Einstein radius R_E , which is given by

$$R_E(M, x) = \sqrt{\frac{4GM}{c^2} D_s x(1-x)}, \quad (2)$$

where M is the lens mass, $x = D_l/D_s$ is the normalized lens distance, and D_l and D_s are the observer-lens and the observer-source star distances, respectively. The time variation of $u = u(t)$ is

$$u(t) = \sqrt{\beta^2 + \left(\frac{t-t_0}{t_E}\right)^2}, \quad (3)$$

where β , t_0 , $t_E = R_E/v_t$, and v_t are the minimum impact parameter in units of R_E , the time of maximum magnification, the event timescale, and the transverse velocity of the lens relative to the line of sight toward the source star, respectively. From a light curve, one can determine the values of β , t_0 , and t_E , but not the values of M , x , or v_t .

Our Microlensing Observations in Astrophysics (MOA) group started observations toward the GB in 1999. From 2000 we introduced the Difference Image Analysis (DIA) (Crotts 1992; Phillips & Davis 1995; Alard & Lupton 1998; Alard 2000; Alcock et al. 1999, 2000; Woźniak 2000; Bond

¹ Princeton University Observatory, Princeton, NJ 08544-1001.

² Solar-Terrestrial Environment Laboratory, Nagoya University, Nagoya 464-8601, Japan.

³ Institute of Astronomy, University of Edinburgh, Royal Observatory, Edinburgh, UK.

⁴ Carter National Observatory, Wellington, New Zealand.

⁵ School of Chemical and Physical Sciences, Victoria University, Wellington, New Zealand.

⁶ Department of Physics and Astronomy, University of Canterbury, Christchurch, New Zealand.

⁷ Institute of Cosmic Ray Research, University of Tokyo, Chiba 277-0882, Japan.

⁸ National Astronomical Observatory, 2-21-1 Osawa, Mitaka, Tokyo 181-8588, Japan.

⁹ Department of Physics, Kyoto University, Kyoto 606-8502, Japan.

¹⁰ Department of Physics, Niigata University, Niigata 950-2181, Japan.

¹¹ Nagano National College of Technology, Nagano, Japan.

¹² Department of Physics, University of Auckland, Auckland, New Zealand.

¹³ Tokyo Metropolitan College of Aeronautics, Tokyo 140-0011, Japan.

¹⁴ Department of Physics, Kounan University, Koube 658-8501, Japan.

¹⁵ Astronomical Institute, Tohoku University, Sendai 980-8578, Japan.

¹⁶ National Aerospace Laboratory of Japan, Tokyo 182-8522, Japan.

et al. 2001), which is able to perform better photometry than the traditional DoPHOT (Schechter, Mateo, & Saha 1993) type analysis in crowded fields at any place, even where no star was identified.

To date, hundreds of microlensing events have been detected toward the GB by the OGLE (Udalski et al. 1994, 2000; Woźniak et al. 2001) and MACHO collaborations (Alcock et al. 1997a, 2000). They estimate the microlensing optical depth toward the GB to be $3.3 \pm 1.2 \times 10^{-6}$ from nine events by DoPHOT analysis, $3.9^{+1.8}_{-1.2} \times 10^{-6}$ from 13 events in a clump giant subsample from DoPHOT, and $3.23^{+0.52}_{-0.50} \times 10^{-6}$ from 99 events by DIA, respectively. Popowski et al. (2001) and Popowski (2002) estimate values of $2.0^{+0.4}_{-0.4} \times 10^{-6}$ and $2.23^{+0.38}_{-0.35} \times 10^{-6}$, respectively, from MACHO data. These values are all more than twice those expected from existing Galactic models, which are somewhere around $0.5\text{--}1.0 \times 10^{-6}$ (Paczynski 1991; Griest et al. 1991; Kiraga & Paczyński 1994). This suggests that the standard models of the Galaxy need to be revised. To explain the high optical depth, a number of authors have suggested the presence of a bar oriented along our line of sight to the GB (Paczynski et al. 1994; Zhao, Spergel, & Rich 1995), and have adopted various values of the bar orientation and mass (Paczynski et al. 1994; Peale 1998; Zhao & Mao 1996). Microlensing observations toward the GB therefore appear useful for characterizing the mass and inclination of the bar.

Popowski et al. (2001) and Popowski (2002) raised the possibility of a systematic bias in the optical depth due to the difficulties of measuring t_E associated with blending and unresolved sources. When the actual source baseline flux is unknown, t_E and β are degenerate in relatively low signal-to-noise ratio (S/N) events (cf. Han 1999; Bond et al. 2001; Gould & An 2002). The optical depth may be estimated by using red clump giant stars to avoid the bias, or by other methods (e.g., Gondolo 1999; Kerins et al. 2001). In this paper, we quantify the bias by using Monte Carlo simulations and take it into account in estimating the optical depth.

Our observations are designed to detect efficient high-magnification events with faint source stars for the study of extrasolar planets and surface-transit events, by increasing the sampling rate up to ~ 6 times per night (note that the sampling rate of other projects is typically once per night). Our observations are consequently fairly sensitive to short-duration events, i.e., events caused by smaller mass lenses. This could lead to a different optical depth estimate from previous studies if there is a significant contribution of low-mass objects such as brown dwarfs to the microlensing optical depth. Thus, the MOA observations, presented here, could constrain the contribution of the low-mass population and also the structure of the GB.

This paper gives the results of the DIA analysis of data toward the GB obtained by MOA in 2000. The aim of the analysis is to find out how efficiently we can detect high-magnification events and short-timescale events, and to estimate the optical depth toward the GB. In § 2 we describe our observations. Section 3 is devoted to the analysis method. In § 4 we describe the event-selection process and results. In § 5 we make an I -band extinction map of our GB fields caused by dust. This is useful in estimating extinction-free source magnitudes in the simulation. In § 6 we describe the simulation used to estimate our detection efficiency and the resulting microlensing optical depth. A discussion and conclusions are given in § 8.

2. OBSERVATIONS

We observed from the Mount John University Observatory (MJUO) in New Zealand at $170^\circ 27' 9''$ E, $43^\circ 59' 2''$ S, 1030 m altitude. Typical sky background values are 21.9, 22.6, 21.5, 20.9, and 19.1 mag arcsec $^{-2}$ in the U , B , V , R_C , and I_C passbands, respectively, at an air mass of 1.0 (A. Gilmore 1994, private communication). Spectroscopic hours are $\sim 45\%$.

We used a 61 cm telescope equipped with the large mosaic CCD camera MOA-cam2 (Yanagisawa 2000). This has three $2k \times 4k$ pixel thinned CCDs. The combined field of view of the camera and telescope is $0^\circ 92' \times 1^\circ 39'$ ($0''.81$ pixel $^{-1}$). We used two nonstandard wide-passband red (630–1100 nm) and blue (400–630 nm) filters. The global seeing is typically $1''.9\text{--}3''.5$.

We observed 14 GB fields (18 deg 2) 3–6 times per night during the southern winter season (from April to November), where each field consists of three subfields corresponding to each CCD. The main aim of the observations was to detect high-magnification events in order to find extrasolar planets (Bond et al. 2001). The detection probability of extrasolar planets in high-magnification events is high (Griest & Safizadeh 1998).

Microlensing events in which the source star is fainter than the observational limiting magnitude are generally known as “pixel lensing” events (Gould 1996) or “EAGLE events” (Nakamura & Nishi 1998; Sumi & Honma 2000). These usually have high magnification. However, the period in which they are visible is very short, because they are visible only at peak magnification. To detect this kind of events we sample each field 5–6 times per day, mainly through the red filter rather than both colors. Because of this high sampling rate, the detection efficiency for short-timescale events is also higher than in former studies. A unique feature of our observations is the ability to detect small lens objects toward the GB.

3. DATA ANALYSIS

We have used the DIA technique to provide sensitivity to pixel lensing or EAGLE events. These events cannot be detected by the conventional (fixed position) DoPHOT-type photometry.

We developed our own implementation of the DIA method of Alard & Lupton (1998) and Alard (2000), which directly models the kernel in real space with spatial variations of the kernel across the CCD. This method is suitable even for crowded and poor S/N images. In this technique, one first registers some star positions, and geometrically aligns each “current” observation image to a preselected “reference” image, which is recorded in good seeing, high S/N, and low air mass. Next, the convolution kernel that is required to map the reference image to the current image is calculated by using the current and reference images. The reference images are convolved to match the seeing and scaled to align with the current images. The resulting images are then subtracted and variable objects are detected.

The images were analyzed in real time at MJUO to issue alerts for the events (Bond et al. 2001). In this analysis we use the same sample of subtracted images as in the real-time analysis.

We have found that the effect of differential refraction, which causes a significant residual flux in the subtracted

image (Tomany & Crotts 1996; Alcock et al. 1999), is negligible in our images with the red filter when the air mass is lower than 2.0. We have not corrected for this effect because our data are mainly taken through the red filter.

We have made a catalog of all stars in the reference images by using DoPHOT. All saturated stars and bad pixels on the reference images are masked out the same as in the subtraction process. These are useful in the following analyses.

3.1. Identification of Variable Objects

On a subtracted image, variable objects can be seen as positive or negative profiles, depending on whether the flux has increased or decreased relative to the reference image. To detect these objects, we use our implementation of the algorithm in the IRAF task DAOFIND, in which both positive and negative profiles can be detected simultaneously. There are also spurious profiles not associated with stellar variability, for example, cosmic rays, satellite tracks, and electrons leaked from bright saturated star images. To avoid detecting these spurious objects, we apply several criteria for the statistics and profiles in the analog digital unit (ADU) value of pixels around the peak, e.g., the S/N is required to be larger than 3.

Candidate objects that pass these criteria are checked against those obtained in previous reductions of the field. If no object is cross-referenced, these new objects are added to the initial list of variable object positions. If an object has previously been detected, this is identified as the same object and the number of detections for this object is incremented. The number of detections for each object is used in the event-selection cut, “cut 1” (see § 4.1.1).

3.2. Photometry

To the list of variable objects made in the previous section, we have applied the first simple event-selection cut 1 (see § 4.1.1) to cull the number of spurious objects in this list. For the objects that passed the cut 1 test, we have performed point-spread function (PSF) profile-fitting photometry, where the high-S/N empirical PSF images (23×23 pixels) are made for each of the 32 (500×500 pixels) subregions in the reference image. Then these PSF images are convolved by the same kernel function used in the subtraction process, to match this PSF to that in each local position of each time series of frames. The total flux of this PSF is normalized to 1.

The PSF photometry comes down to a two-parameter fit for the amplitude, a_{PSF} , and baseline b , i.e., $a_{\text{PSF}}\text{PSF}_i + b$, where PSF_i is the value of empirical PSF image in pixel i centered on the variable object. In principal, in subtracted images, the background is zero by virtue of the least-square process. However, in fact there are residuals, especially around the very bright saturated stars, bright variable stars, and in poor S/N images. In our images, the fraction of the area in which these effects occurs is small but not negligible, because of the wide wing of the PSF (our median seeing is about $2''/3$). When we compare the one- and two-parameter fits, we find that several faint stars around a bright variable star show variability similar to that of the bright variable star in the one-parameter fit, but not in the two-parameter fit. Fitting a second “baseline flux” parameter on the subtracted images provides a good zero-point check, so we make the baseline b a fitting parameter. In the subtracted

images the flux has been rescaled to match that in the reference image by dividing with the scale factor a_0 , which is the first coefficient of the kernel function of the frame. By this process, all the time series of subtracted images are photometrically calibrated. Then no extinction correction is required. In the fitting, the noise of each pixel σ_i of the subtracted image is given from the actual flux f_i in the current image before subtraction, taking into account the gain G in ADU/e^- and the scale factor a_0 of each frame.

This photometry has been performed on all objects in the variable list in all the time series of images and the differential flux $\Delta F = a_{\text{PSF}}$ light curves stored in the database, with their corresponding error and the square root of the reduced χ^2 in the PSF fitting (we refer to this as Sdev_{PSF}).

3.2.1. Noise Properties

The error in the PSF photometry, σ_{PSF} , obtained by χ^2 fitting should be optimistic, as it includes only the photon noise component, so we test the properties of the photometry using a sample of constant stars. We have randomly sampled ~ 1000 constant stars for each image in our star catalog, from which we have rejected the variable objects detected in § 3.1.

Noise properties are derived from the residuals of individual measurements around the mean flux of each object. We thus use $\sim 100,000$ measurements for each chip. Each residual is normalized by the error from the photon noise σ_{PSF} for the corresponding photometric point. Then stars are grouped according to their brightness on the reference image, the standard deviation normalized by σ_{PSF} in the PSF fitting, i.e., Sdev_{PSF} . We think that the Sdev_{PSF} of each measurement should be a good indicator for the systematic noise, which comes from the non-photon noise. All residuals coming from the light curves of stars in a given group are merged into one distribution.

For each group we calculate the half-width of the region containing 68.3% of residuals, σ_{resid} , a robust estimator of the width σ of the Gaussian distribution. In Figure 1, we plot the estimated σ_{resid} as a function of Sdev_{PSF} , and these are fitted with a three-degree polynomial. Here bright stars

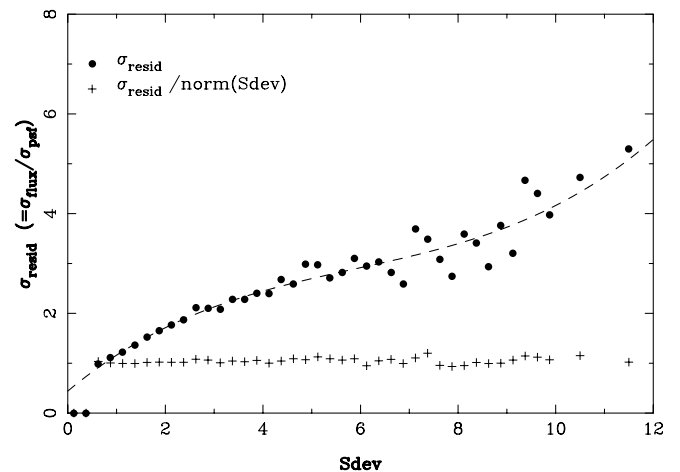


FIG. 1.—Half-width of the region containing 68% of residuals, which are a ratio of the actual scatter to the photon noise estimate as a function of Sdev_{PSF} (filled circles), and the same plot with renormalization (crosses). The dashed line indicates the best fit for the residual plot with a three-degree polynomial.

($R < -11$ in DoPHOT output red magnitude, which corresponds to $I < 15$; see § 3.3) are rejected because such bright stars have other systematic deviations, as discussed below. The effect of such bright stars is small since, in total, they represent less than 0.4% of all possible source stars ($I < 23$), and such stars dominate on less than 1% of the pixels on the CCD chip. We did not use those measurements with $Sdev_{PSF} > 10$, as they are unreliable. The fraction of such measurements is $\sim 7\%$ of all measurements. In this figure, a clear trend for these values can be seen, and the fitted curve can be used to rescale the error bars in order to improve the consistency of the light curves. We also show the same plot normalized with this fitted function in Figure 1.

To check whether this normalization is appropriate or not, we show the distribution histograms of these residuals (*top panel*) and normalized residuals (*bottom panel*) in Figure 2. As shown in this figure, the distribution of normalized residuals is consistent with the normal distribution. So, our normalization seems to be reasonable. This exercise has been carried out for each of the CCD chips, which shows that chips 2 and 3 are very similar but differ slightly from chip 1. We have thus estimated this function for each chip. This trend is very similar over all fields measured with the same CCD chip, and we have applied this normalization to all our measurements.

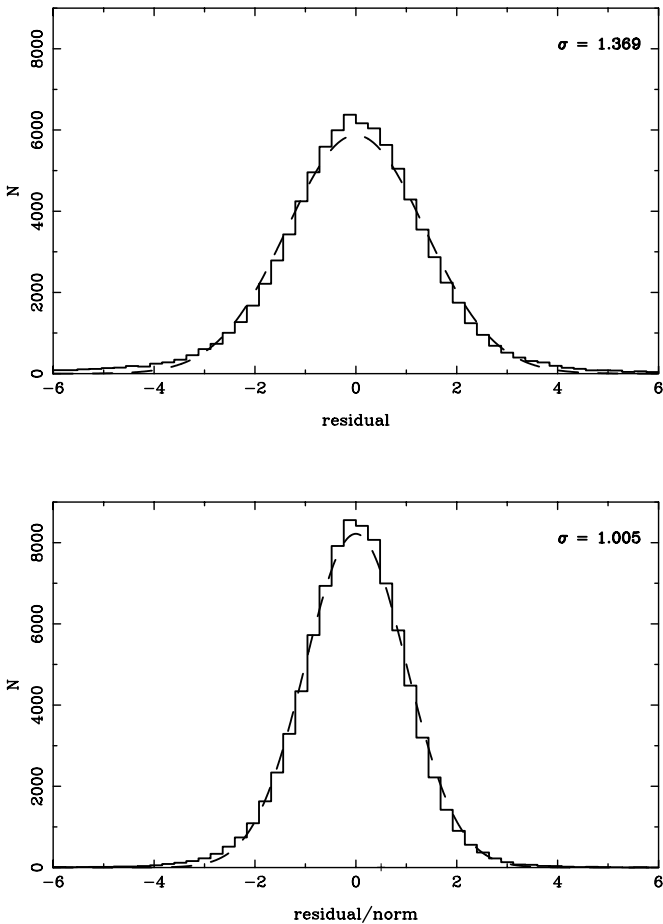


FIG. 2.—Distribution of residuals (*top*) and renormalized residuals (*bottom*) for 90,000 individual measurements of constant stars as histograms. The dashed lines indicate the best-fit Gaussian distributions centered on 0. The half-widths of the regions containing 68% of the residuals σ are 1.369 and 1.005, respectively.

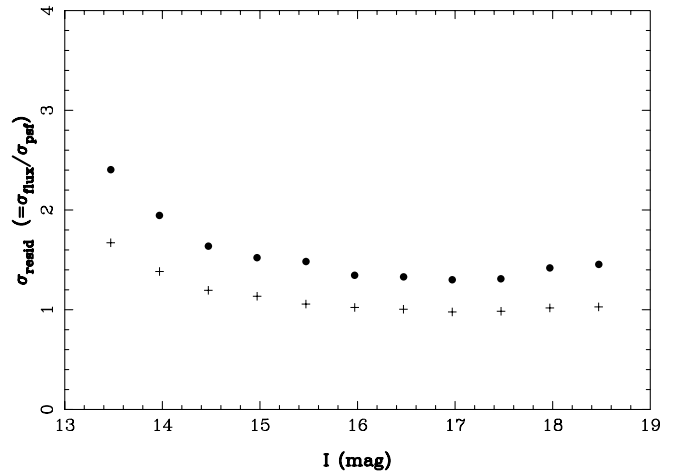


FIG. 3.—Half-width of the region containing 68% of the residuals, which are a ratio of the actual scatter to the error from the photon noise (*filled circles*) as a function of I -band magnitude, and the same plot with renormalization (*crosses*). The data in this plot come from 90,000 individual measurements of 1000 constant stars.

In Figure 3 we show the σ_{resid} of residuals (*filled circle*) and normalized residuals (*cross*) as a function of brightness of constant stars in I -band magnitude (see § 3.3). As shown in Figure 3, as we move toward brighter stars the σ_{resid} increases because of systematic effects related to the uncertainty in the seeing and the PSF, first slowly and then faster. Alard & Lupton (1998) provide a possible explanation in terms of the atmospheric turbulence. Another possible source of this excess is the existence of some small-amplitude variable stars in these bright stars. No correction for this effect is made in this analysis. In Figure 3, we find that the noise (standard deviation) in this analysis is about 40% above the photon noise limit.

3.3. Calibration of Fluxes

To obtain the source magnitude from the baseline flux f_0 given by light-curve fitting, we need the transformation relation between the flux in the reference image and the apparent magnitude in standard passbands. We use the $UBVI$ photometry catalog of selected stars in Baade's window provided by OGLE (Paczynski et al. 1999), which are contained in three MOA GB subfields (ngb2-1, ngb2-2, and ngb3-3, where ngb2-1 means chip 1 in field ngb2). In these regions, the extinction is relatively low and uniform. Our star catalog has been made by applying DoPHOT to half of all the frames for each field that contains ~ 20 blue images taken during the 2000 season. Then we have made the $R(MOA)$ and $B(MOA)$ catalogs of all stars in our GB fields by taking the median for each star so as to increase the accuracy of the photometry and to avoid the daily difference of extinction by the atmosphere. Then the DoPHOT photometry R_{ref} of the reference images is compared with the catalog value R_{med} . The differences are $R_{ref} - R_{med} = -0.1 \sim +0.03$ mag, and spatial variations in one chip are about ~ 0.02 mag. We have neglected local differences in the chip and stored one offset value for each chip. These offsets are used in the following calibrations.

Next, the R and B measurements in our catalog of three MOA-OGLE overlap fields are compared with the V and I

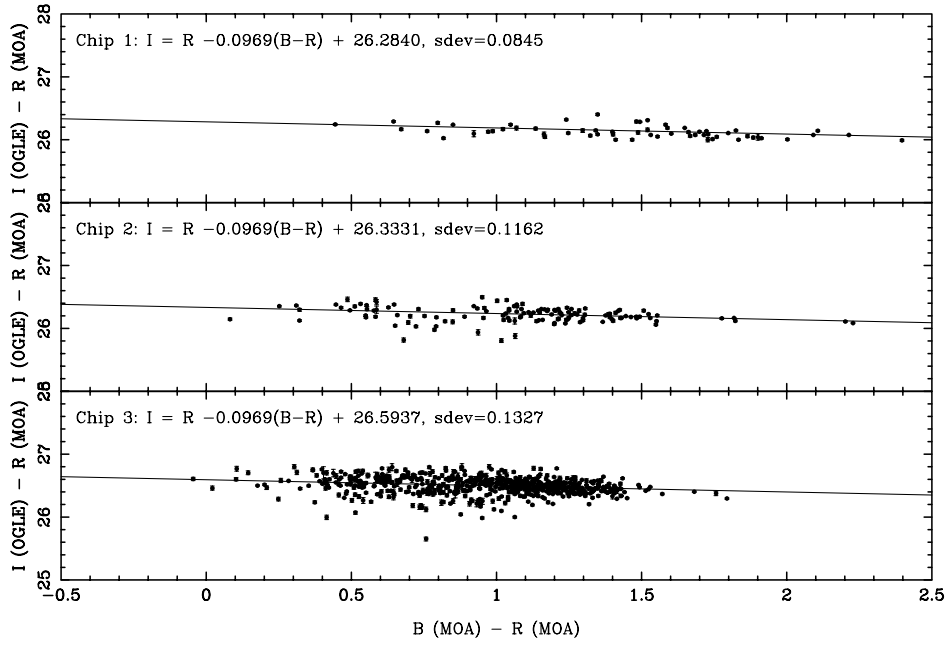


Fig. 4.—Calibration of MOA red measurements to the standard I -band magnitude for the three CCDs (chips 1, 2, and 3 from top to bottom) with the color term.

photometry of the corresponding star in the OGLE catalog. Fundamentally, the transformation to the standard V and I from MOA nonstandard R and B depends on the color index $B-R$. The transformations obtained to the standard I and V for each chip are shown in Figure 4 and 5, and are given by

$$I = R - 0.0969(B - R) + 26.2840 \quad (\text{chip 1}), \quad (4)$$

$$I = R - 0.0969(B - R) + 26.3331 \quad (\text{chip 2}), \quad (5)$$

$$I = R - 0.0969(B - R) + 26.5937 \quad (\text{chip 3}), \quad (6)$$

$$V = B - 0.160(B - R) + 26.350 \quad (\text{chip 1}), \quad (7)$$

$$V = B - 0.160(B - R) + 26.800 \quad (\text{chip 2}), \quad (8)$$

$$V = B - 0.160(B - R) + 26.192 \quad (\text{chip 3}). \quad (9)$$

Here the slopes were estimated by using the full data of all three chips, and the offsets were estimated individually for each chip.

We apply these transformations to our star catalog. As shown in Figure 4, the color dependence in transforming to I from R is weak, and we find that the transformation

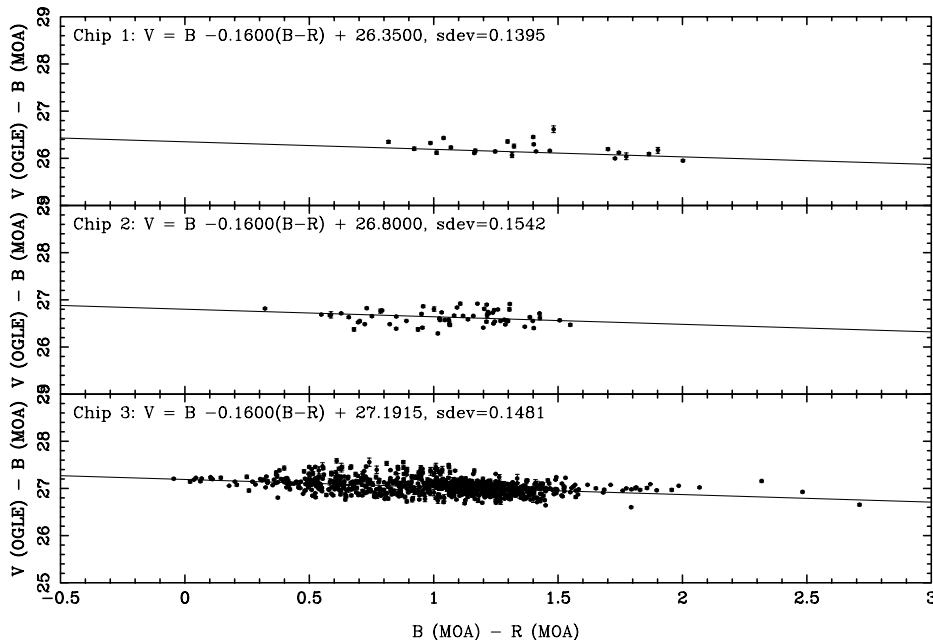


Fig. 5.—Calibration of MOA blue measurements to the standard V -band magnitude scale of the three CCDs of the camera MOA-cam2 with the color term.

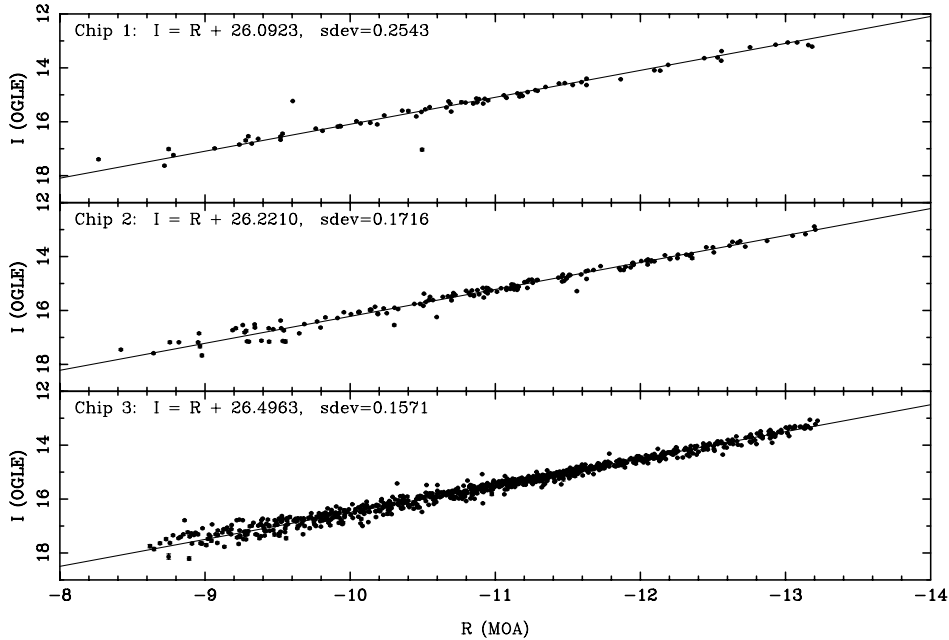


FIG. 6.—Calibration of MOA red measurements to the standard I -band magnitude scale of the three CCDs of the camera MOA-cam2 without a color term.

without a color term seems to work properly, as shown in Figure 6. The transformation functions can be written as

$$I = R + 26.0923 \quad (\text{chip 1}), \quad (10)$$

$$I = R + 26.2210 \quad (\text{chip 2}), \quad (11)$$

$$I = R + 26.4963 \quad (\text{chip 3}). \quad (12)$$

These equations are very useful because our data were usually taken only in red.

4. RESULTS

The data consist of 7200 images (~ 100 Gbyte), which correspond to 118–224 frames for each field, depending on their priority. Of these, 6600 images ($\sim 92\%$) have been successfully reduced. The reduction failures occurred as a result of poor data conditions, i.e., bad pointing, poor seeing, or very low transmission due to clouds.

In these subtracted images we find 2000–10,000 variable objects in each field. Of these variable objects, 200–1000 pass cut 1, for which the PSF photometry is performed to make the light curves. For these light curves, we apply additional selections, i.e., cut 2, which searches for a bump in the light curve, and cut 3, in which microlensing fitting is performed. As a result, we find 28 microlensing event candidates from these light curves.

4.1. Event Selection

We apply a combination of simple selection criteria to reject the various spurious detections and variable stars. These criteria are chosen empirically.

4.1.1. Cut 1

We have applied a simple selection criterion termed the “point cut” for the initial variable objects detected in § 3.1 by using the number of detections of each object in a time

series of frames. There are three types of events in our data set. The first is an event in which the source star is not magnified in the reference frame. The second is an event in which the source star is magnified to its maximum amount relative to the reference image. The third is in between, i.e., the source star is magnified but not at the peak magnification relative to the reference image. For events of type 1, objects are detected only when the source is magnified as a positive excess. For type 2, objects are detected in almost all frames except around the peak as a negative excess. For type 3, the same excess as for types 1 and 2, or the combination of a cluster of positive excesses at the peak and a negative baseline, are detected depending on the phase of magnification in the reference image.

First we count the number of clusters of positive and negative detections, $N_{\text{clus},p}$ and $N_{\text{clus},n}$, which are consecutive detections separated by less than 4 observation frames.

For type 1 events that have no negative detections, $N_{\text{det},n} = 0$, the positive detection should be larger than 2, i.e., $N_{\text{det},p} \geq 2$, which rejects many spurious detections and low-S/N events. The $N_{\text{clus},p}$ should be less than 4 to reject short-period variables, and $N_{\text{det},p}$ should not be equal to $N_{\text{clus},p}$, to reject objects with noisy, sparse detections. We divide all frames into three regions of observation time, and calculate the detection $\text{Ratio}_{1,2,3}$, which is the number of detections $N_{\text{det},1,2,3}$ out of all observation frames $N_{\text{frame},1,2,3}$. We require that the $\text{Ratio}_1 \leq 0.1$ or $\text{Ratio}_3 \leq 0.1$, to reject some of the long- or middle-period variables.

For type 2 events that have no positive detection, $N_{\text{det},p} = 0$, the negative detection should be larger than a quarter of all observation frames, i.e., $N_{\text{det},n} \geq N_{\text{frame}}/4$, because these negative detections represent the baseline. The $N_{\text{clus},n}$ should be less than 5 to reject short-period variables, because the baseline should be stable.

For type 3 events, which have both positive and negative detections, $N_{\text{clus},p}$ should be less than 4, and $N_{\text{clus},n}$ should be less than 5 to reject short-period variables, the same as

TABLE 1
SELECTION CRITERIA IN CUT 1

Type	Criteria
Type 1	$N_{\text{det},n} = 0$ $N_{\text{det},p} \geq 2$ $N_{\text{clus},p} < 4$ $N_{\text{det},p} \neq N_{\text{clus},p}$ $\text{Ratio}_1 \leq 0.1$ or $\text{Ratio}_3 \leq 0.1$
Type 2	$N_{\text{det},p} = 0$ $N_{\text{det},n} \geq N_{\text{frame}}/4$ $N_{\text{clus},n} < 5$
Type 3	$N_{\text{det},n} \neq 0$ and $N_{\text{det},p} \neq 0$ $N_{\text{clus},p} < 4$ $N_{\text{clus},n} < 5$ $(N_{\text{det},p} \geq 2$ and $N_{\text{det},p} \neq N_{\text{clus},p})$ or $N_{\text{det},n} \geq N_{\text{frame}}/4$

for type 1 and 2 events. Either of the criteria for type 1, $N_{\text{det},p} \geq 2$ and $N_{\text{det},p} \neq N_{\text{clus},p}$, or for type 2, $N_{\text{det},n} \geq N_{\text{frame}}/4$, should be satisfied. We list all the criteria of cut 1 in Table 1.

These cuts reduce the variable objects from thousands (2000–10,000) to hundreds (200–1000), depending on each field, without rejecting the microlensing-like light curves. For these objects the PSF photometry is performed to construct light curves.

4.1.2. Cut 2

The second cut, cut 2, has been applied to the light curves of objects that pass cut 1. This cut searches for a microlensing-like ‘‘bump’’ on the stable baseline in the light curve.

First, we require that the number of photometric data points, N_{total} , should be ≥ 70 points. Next, we set the time interval of 120 days as a ‘‘window’’ in the light curve, where the number of data points in the window, N_{in} , and outside the window, N_{out} , is required to be more than three and nine points, respectively. In this window, we count the number of peaks, N_{peak} , which is defined to be that consecutive excess whose significance is larger than 2.5σ , and the significance of at least two of these points should be larger than 4σ . Here the significance of each photometric point is calculated as

$$\sigma_i = \frac{f_i - f_{\text{med,out}}}{\sqrt{\sigma_{f,i}^2 + \sigma_{\text{out}}^2}}, \quad (13)$$

where f_i and $\sigma_{f,i}$ are the flux and error of the i th data point, and $f_{\text{med,out}}$ and σ_{out} are the median and variance of data points outside the window, respectively.

The N_{peak} is required to satisfy $1 \leq N_{\text{peak}} \leq 3$, and the maximum of the sum of the significance of the points in each peak, $\sum_{i,\text{peak}} \sigma_i$, should be larger than 20. We define a high excess as one or more consecutive data points whose significance is larger than 2.5σ , i.e., all excesses including ‘‘peak’’ defined above and one that is not significant to categorize as a peak. The number of the high excesses, N_{hi} , in the window should be less than six, which rejects short-period variables and noisy light curves. We require that the reduced χ^2 of data outside the window, χ_{out}^2 , should be less than 4. But if the ratio of χ^2 inside and outside the window, $\chi_{\text{in}}^2/\chi_{\text{out}}^2$, is larger than 15, the cut with χ_{out}^2 is not required, so as to allow the high-S/N long-duration events to pass. We list all these criteria of cut 2 in Table 2.

TABLE 2
SELECTION CRITERIA IN CUT 2

Criteria
$N_{\text{total}} \geq 70$
$N_{\text{in}} > 3$
$N_{\text{out}} > 9$
$1 \leq N_{\text{peak}} \leq 3$
$\sum_{i,\text{peak}} \sigma_i \geq 20$
$N_{\text{hi}} < 6$
$\chi_{\text{out}}^2 < 4$ or $\chi_{\text{in}}^2/\chi_{\text{out}}^2 \geq 15$

With this cut, 24,543 light curves have been reduced to 1014 in all our GB fields.

4.1.3. Cut 3

For the light curves that passed cut 2, the microlensing model fitting with equation (1) has been applied in cut 3. In DoPHOT analysis the fittings are performed with the background blending flux F_b , i.e., $F(t) = F_0A(t) + F_b$, where F_0 indicates a baseline source flux. However, in DIA we observe only the variation of the flux from that in the reference image, as

$$\Delta F(t) = F_0A(t) - F_0A(t_{\text{ref}}), \quad (14)$$

where t and t_{ref} are the time when the current and the reference image are taken, respectively. The F_b is canceled out in this formula. Equation (14) with four parameters ($F_0, t_0, u_{\text{min}}, t_E$) is fitted to differential flux ΔF light curves in this cut 3.

The reduced χ^2 in a microlensing fit are required to be less than 3.5 to reject most long-period variables (LPVs) and noisy light curves, although very high S/N events are sometimes not well fitted by the standard microlensing model because of exotic effects such as parallax. Thus, for the events whose peak flux is larger than 450,000 ADU, we require $\chi^2 < 100$ instead of $\chi^2 < 3.5$. The event ngb1-2-2717 falls into this category because of the parallax effect. After these cuts, 75 light curves still remain, most of which have a clear single peak and stable baseline. These are microlensing candidates, dwarf novae (DNe), and low-S/N faint LPVs.

The main background in this event selection are DNe, which can be well fitted by microlensing in the case of poor sampling. In our light curves that passed cut 1, 20 light curves are clearly identified as DNe. These have single or sometimes multiple asymmetric flares in the light curve, which usually rise quickly and fade slowly.

To check whether an object is a DN or not, we cross-referenced to the existing light curves in the MACHO group’s database,¹⁷ whose fields overlap some of ours, and found other flares in the light curves of five objects; these are clearly DNe. The DNe are much bluer during outburst. However, we usually observe only with the red filter to increase the sampling rate, and only rarely observe with the blue (only ~ 30 frames for each field). For 23 out of these 75 candidates, we could measure the

¹⁷ See <http://www.macho.mcmaster.ca>.

color during the flare. Five of these 23 candidates are categorized as DNe because they are very blue ($V - I \leq 1.0$). In 15 light curves, including 5 of the above 10 DNe, asymmetric flares are clearly seen. In total, 20 objects are categorized as DNe.

Two of these DNe are rejected at cut 2, and one DN is removed at χ^2 by cut 3. To reject other DNe, we are unable to use a color cut because we have no color information in most of the light curves. On the other hand, we have frequent sampling data points for these objects, which makes it easier to identify a DN from the shape. We also find that the following cuts would reject almost all DNe in addition to LPVs. First, the minimum impact parameter u_{\min} should be less than 1; 15 DNe are fitted with a large u_{\min} . Some LPVs are also cut here. Furthermore, we impose the condition that the timescale should be $0.3 < t_E < 200$ days. Two further DNe are rejected here, which are fitted to very large event timescales ($t_E > 1000$ days). In consequence, all DNe that have been clearly identified are rejected by these cuts. Although five of these have been identified as DNe not by a clear shape of the flare but by their color or by the existence of other flares in past data, which can be done randomly, these are rejected by our cuts. These results give us the confidence that all DNe are rejected by these cuts. Even if a few DNe are not rejected, it should not be a significant fraction in our results. At the same time, nine microlensing-like light curves, which could not be clearly identified as either DNe or microlensing events, are rejected with this cut.

In microlensing events measured only around the peak or with low S/N, t_E and u_{\min} would be degenerate (Han 2000), so some real microlensing events might be removed at this cut. These effects are also seen for the artificial events with faint source stars in our simulation (see § 6.3). If both the colors are taken simultaneously or the catalog of DNe is used, we can easily distinguish real microlensing events from DNe and issue the alerts. Such events are usually high-magnification events because their source star is very faint. If the baseline flux is measured by follow-up observations with larger high-resolution telescope such as the *Hubble Space Telescope* (*HST*) or VLT, the timescale is well constrained. Other LPVs are also cut here.

Thirty-one objects have passed these criteria. In these light curves, three low-S/N LPVs still remain. We have rejected these LPVs directly, as we are doing in real-time analysis (Bond et al. 2001), instead of imposing more complicated criteria. In real-time analysis we have made a list of variables, and objects that cross-reference to these variables are rejected. This treatment does not affect the optical depth estimation, because that is position-dependent and these positions are rejected in the following analysis. We list all the criteria of cut 3 in Table 3.

TABLE 3
SELECTION CRITERIA IN CUT 3

Criteria
$\chi^2/\text{dof} < 3.5$ for $F_{\text{peak}} < 450,000$ ADU
$\chi^2/\text{dof} < 100$ for $F_{\text{peak}} > 450,000$ ADU
$u_{\min} < 1$
$0.3 < t_E < 200$ day

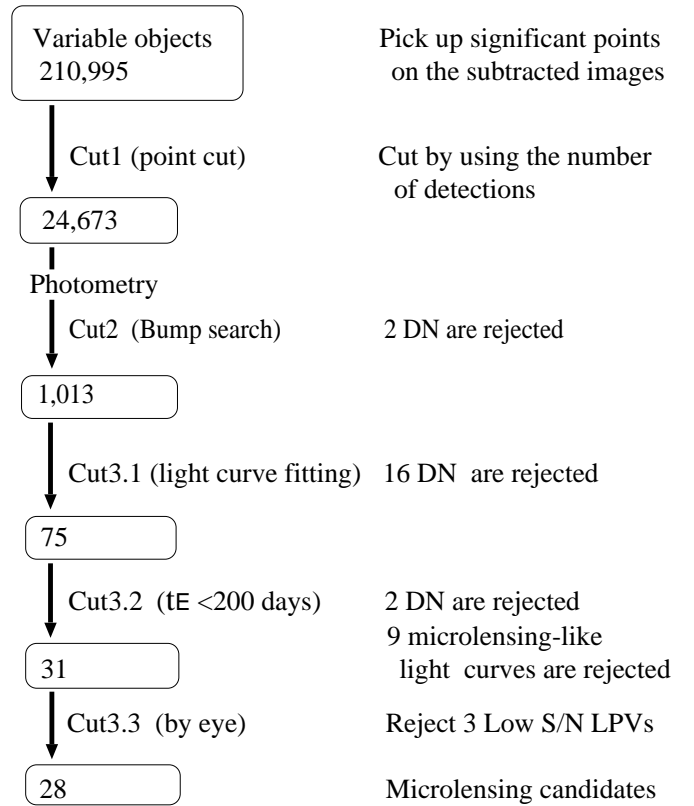


FIG. 7.—Flowchart of the procedure for selecting microlensing candidates.

As a result, we find 28 microlensing candidates in our GB database during 2000. We confirmed that these 28 candidates did not have any significant variability during the following two seasons (in 2001 and 2002). Three out of 20 candidates reported in real-time analysis (Bond et al. 2001) have failed in this off-line analysis because the t_E are not well constrained. Furthermore, 11 new candidates are found because we have changed the threshold to detect variable objects on the subtracted images in § 3.1. We summarize the event-selection processes in Figure 7.

We show light curves of these 28 candidates in Figures 8–10, where the ΔF data points have been converted to amplifications using the fitted parameters. The gap around $\text{JD} = 2,451,750$ in the light curves is due to the malfunctioning of our camera system for ~ 40 days.

We list the positions of all candidates with ID in this analysis in Table 4. The ID in real-time analysis and alert ID reported in Bond et al. (2001) are also tabulated. We list the best-fit microlensing parameters and 1σ lower and upper limits in Table 5. The I -band baseline magnitude of the source star, I_0 , is dereddened to match the *HST* field by using the I -band extinction, A_I , map of each field. These fitted parameters are not biased by the blending effects due to nearby stars, which appear in DoPHOT-type analyses (Udalski et al. 1994; Alcock et al. 1997a, 1997b) and would make t_E shorter. In DIA all other blending components can be subtracted.

The light curve of the event ngb1-2-4925 exhibits an asymmetric profile due to the effect of parallax. The best-fit parameters in fitting with parallax microlensing models for this event are presented in Bond et al. (2001). We use these values for the following optical depth estimation.

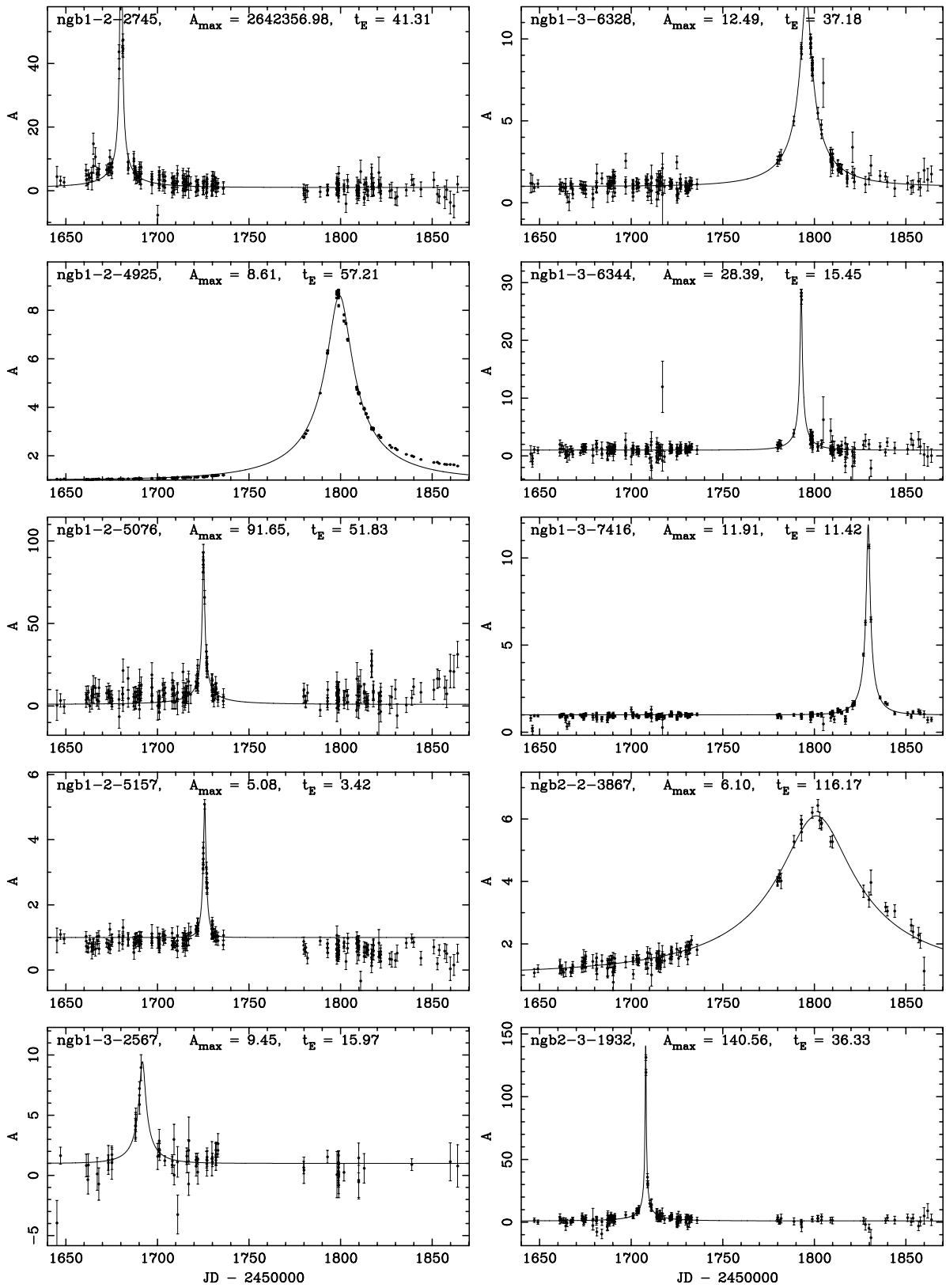


FIG. 8.—Light curves of microlensing event candidates

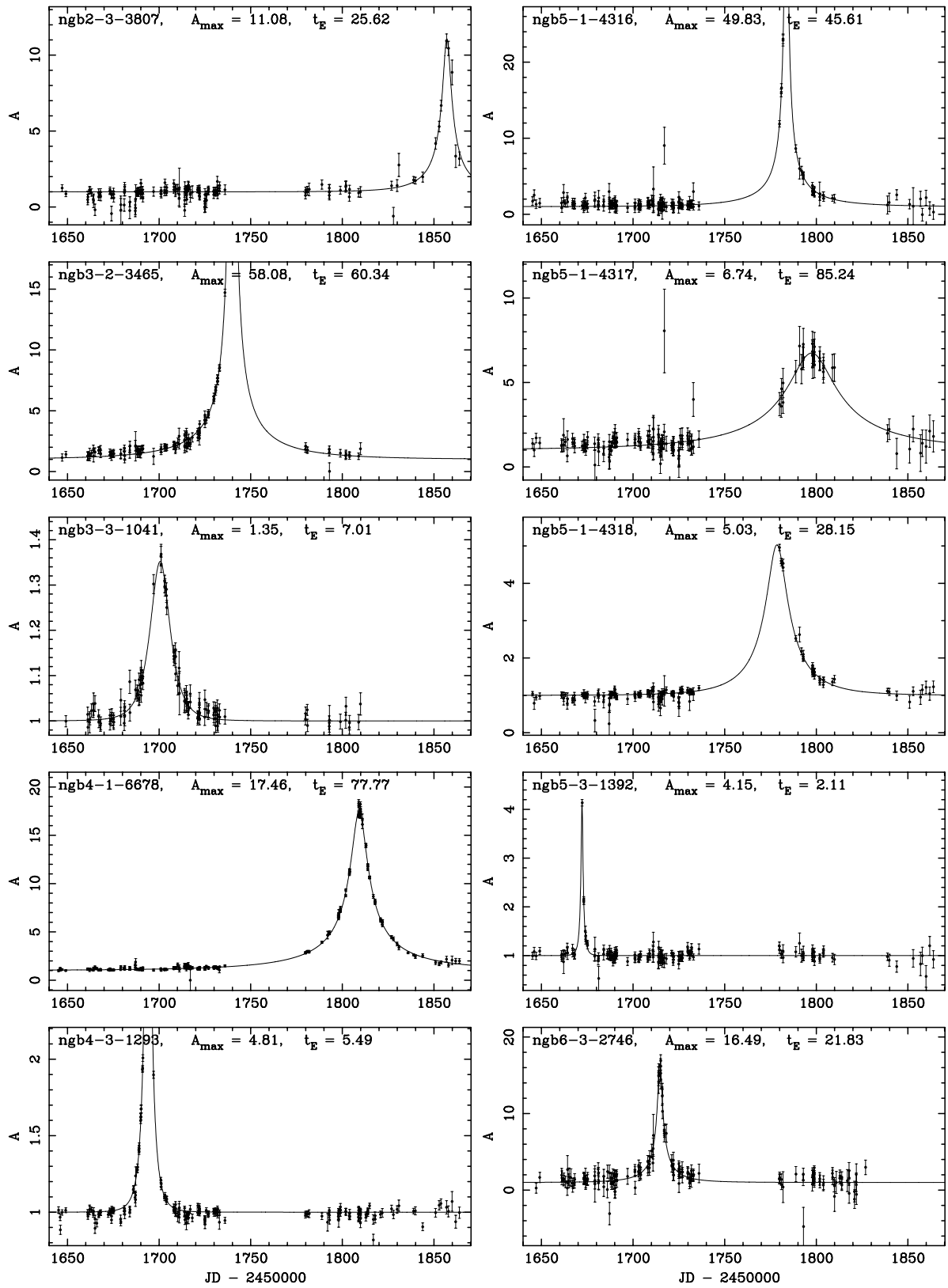


FIG. 9.—Light curves of microlensing event candidates

TABLE 4
POSITION OF 28 MICROLENSING EVENT CANDIDATES

Field	Chip	ID	ID (Real Time)	ID (Alert)	R.A. (J2000)	Decl. (J2000)
ngb1.....	2	2745	17 58 13.136	-29 09 14.23
ngb1.....	2	4925	2717	2000-BLG-11	17 57 07.907	-29 09 59.28
ngb1.....	2	5076	17 56 33.952	-29 27 16.08
ngb1.....	2	5157	2667	2000-BLG-7	17 54 56.681	-29 31 47.50
ngb1.....	3	2567	727	2000-BLG-3	17 54 29.770	-28 55 59.31
ngb1.....	3	6328	2540	...	17 58 20.936	-28 47 48.76
ngb1.....	3	6344	2548	...	17 55 05.425	-28 50 34.60
ngb1.....	3	7416	17 57 54.728	-28 54 32.66
ngb2.....	2	3867	1648	...	18 00 12.361	-29 37 23.93
ngb2.....	3	1932	17 59 00.087	-29 33 01.11
ngb2.....	3	3807	18 00 07.092	-29 23 27.47
ngb3.....	2	3465	1316	2000-BLG-9	18 05 09.533	-30 36 06.77
ngb3.....	3	1041	18 06 47.640	-29 50 09.57
ngb4.....	1	6678	2806	2000-BLG-13	17 55 33.202	-28 10 17.09
ngb4.....	3	1293	159	...	17 57 47.197	-27 33 52.80
ngb5.....	1	4316	1673	...	18 01 06.711	-28 52 22.28
ngb5.....	1	4317	1672	...	18 01 26.814	-28 52 34.66
ngb5.....	1	4318	1668	...	18 01 44.791	-28 58 03.53
ngb5.....	3	1392	18 01 21.393	-28 02 51.70
ngb6.....	3	2746	18 04 46.138	-28 31 31.54
ngb6.....	3	3954	1425	2000-BLG-12	18 03 54.776	-28 34 58.62
ngb7.....	3	2192	703	2000-BLG-8	18 10 55.621	-29 03 54.20
ngb9.....	3	2336	841	...	18 10 17.990	-27 31 19.31
ngb10.....	1	1837	18 08 32.453	-26 09 29.66
ngb10.....	3	2112	18 08 51.926	-25 24 40.46
ngb11.....	2	1594	1142	2000-BLG-10	18 11 28.310	-26 15 05.81
ngb11.....	3	1063	18 11 57.020	-25 54 57.32
ngb12.....	2	3187	1052	...	18 14 47.421	-25 32 53.64

NOTE.—ID in this offline analysis, ID in real-time analysis, and alert ID in Bond et al. 2001 are also presented.

5. EXTINCTION MAP

As is well known, the extinction due to dust is very significant toward the GB. This effect can be seen in our color-magnitude diagram (CMD) of the field near

Baade’s window (*left panel*) and another high-extinction field (*middle panel*) in Figure 11. The CMD is more scattered in the high-extinction field than in the Baade’s window field because of the extinction and the reddening. Information on the extinction in each region is needed to

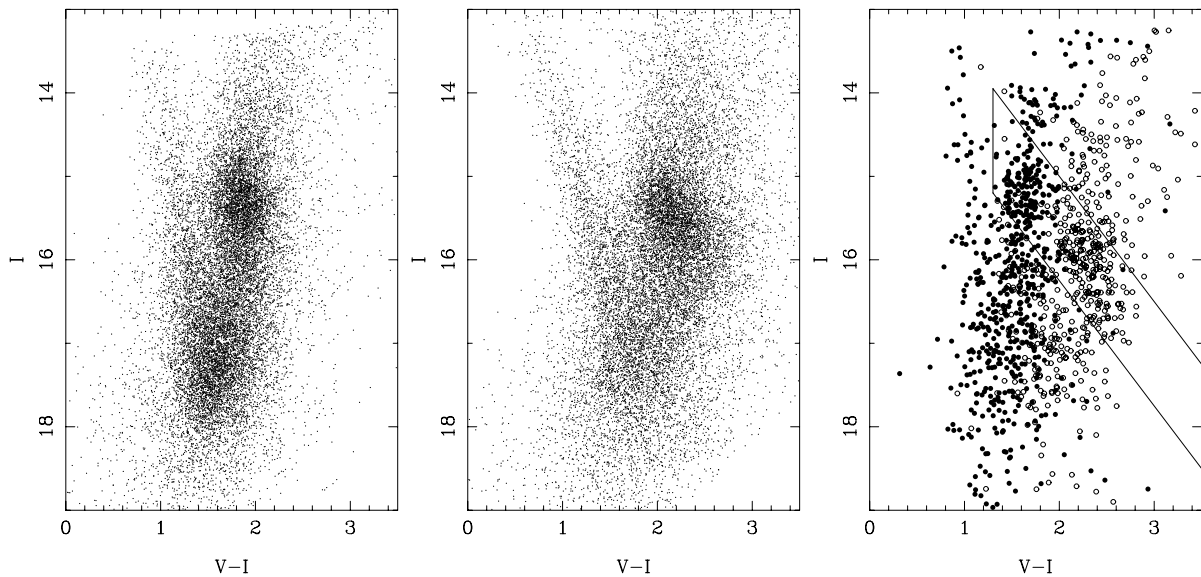


FIG. 11.—CMD of the Baade’s window field (*left*), a higher extinction field (*middle*), and two subregions in the Baade’s window field (*right*). The extinction A_I in each subregion (*right panel*) are 0.761 (*filled circles*) and 1.645 (*open circles*). The box in the right panel encloses the red clump giant region defined by $I - 1.5(V - I) = 1.2, 13.25$.

TABLE 5
PARAMETERS IN MICROLENSING LIGHT CURVE FITTING FOR 28 CANDIDATES

MOA ID			t_0 (JD - 2,450,000)	A_{\max}			t_E (days)			I_0 (mag)
Field	Chip	ID		Lower	Best	Upper	Lower	Best	Upper	
ngb1.....	2	2745	1680.16	200.0	2.6×10^6	8.8×10^8	26.9	41.3	...	19.7
ngb1.....	2	4925	1799.38	8.5	8.6	8.7	56.9	57.2	57.5	13.6
ngb1.....	2	5076	1725.17	56.1	91.7	234.4	33.2	51.8	106.4	20.8
ngb1.....	2	5157	1725.79	4.1	5.1	6.2	2.9	3.4	4.0	17.1
ngb1.....	3	2567	1691.82	2.9	9.4	293.9	6.9	16.0	...	17.5
ngb1.....	3	6328	1795.55	9.4	12.5	16.8	30.6	37.2	45.9	17.6
ngb1.....	3	6344	1792.80	14.9	28.4	60.3	10.0	15.4	27.3	18.3
ngb1.....	3	7416	1829.40	10.6	11.9	13.2	10.6	11.4	12.2	16.2
ngb2.....	2	3867	1801.09	4.6	6.1	9.1	92.0	116.2	163.6	17.4
ngb2.....	3	1932	1707.91	76.5	140.6	361.4	21.1	36.3	181.2	19.9
ngb2.....	3	3807	1857.06	7.2	11.1	17.6	18.1	25.6	37.9	17.8
ngb3.....	2	3465	1739.96	28.7	58.1	115.9	45.9	60.3	269.2	18.8
ngb3.....	3	1041	1700.57	1.2	1.4	1.9	0.3	7.0	9.6	15.1
ngb4.....	1	6678	1809.17	16.4	17.5	18.6	73.4	77.8	82.4	16.2
ngb4.....	3	1293	1693.95	3.0	4.8	12.8	4.8	5.5	6.2	14.5
ngb5.....	1	4316	1783.60	33.5	49.8	89.0	35.2	45.6	62.8	18.1
ngb5.....	1	4317	1797.46	3.8	6.7	16.9	55.2	85.2	188.2	17.9
ngb5.....	1	4318	1778.51	3.3	5.0	6.8	22.0	28.2	34.2	16.0
ngb5.....	3	1392	1672.15	2.4	4.1	5.8	1.6	2.1	3.0	16.5
ngb6.....	3	2746	1714.69	11.5	16.5	24.6	16.3	21.8	30.9	19.7
ngb6.....	3	3954	1796.00	6.5	7.5	8.8	12.4	13.4	14.5	16.5
ngb7.....	3	2192	1732.84	1.5	1.7	1.8	12.7	13.5	14.4	14.6
ngb9.....	3	2336	1792.14	1.2	1.4	1.9	0.8	7.5	10.3	14.1
ngb10.....	1	1837	1663.93	38.2	51.8	71.5	12.7	15.4	19.0	19.0
ngb10.....	3	2112	1700.85	15.0	28.8	...	2.9	5.8	99.4	18.3
ngb11.....	2	1594	1730.46	9.0	9.6	10.4	45.7	48.8	52.3	16.6
ngb11.....	3	1063	1685.29	16.5	27.2	82.4	25.6	38.4	107.1	19.7
ngb12.....	2	3187	1789.45	3.7	4.6	5.6	6.7	7.5	8.2	15.8

NOTE.— I -band baseline magnitude of source star I_0 is dereddened to match the *HST* field by using the I -band extinction A_I map of each field (see § 5). Ellipses indicate that a value could not be constrained.

estimate the number of stars in this region using the luminosity function.

We apply the method of Paczyński et al. (1999), which uses red-clump-dominated parts of the CMDs to determine the offsets caused by differential extinction. They have made a reddening map for their fields because it is easier to determine the reddening E_{V-I} (horizontal shift in CMD) than A_I (vertical shift in CMD). Then the extinction maps are calculated by the formula (Woźniak & Stanek 1996; Ng et al. 1996; Stanek 1996)

$$A_I = 1.5E_{V-I}. \quad (15)$$

We have made CMDs of I versus $(V-I)$ for each of 8×16 subdivided regions (3.45×3.45) by using our star catalog. A sample of these CMDs of different subregions in the image near Baade’s window is shown in the right panel of Figure 11. In this figure, differential reddening is clearly seen. We select the red-clump-giant region in the CMD following Paczyński et al. (1999) as indicated in Figure 11. The parallel lines whose slopes are the reddening vectors (Stanek 1996) are given by

$$I - 1.5(V - I) = 1.2, 13.25. \quad (16)$$

We estimate the mean values of $(V-I)$ and I for red clump giants in each subregion, which correspond to the correlation between differential reddening, $E(V-I)$, and differential extinction, A_I . These values in a field are plotted in

Figure 12, where the best-fitted line is given by

$$I = (1.45 \pm 0.12)(V - I) + 12.7. \quad (17)$$

This slope is consistent with Stanek (1996). The mean color $(V-I)_{\text{mean}}$ is more reliable than I , so we estimate E_{V-I} from

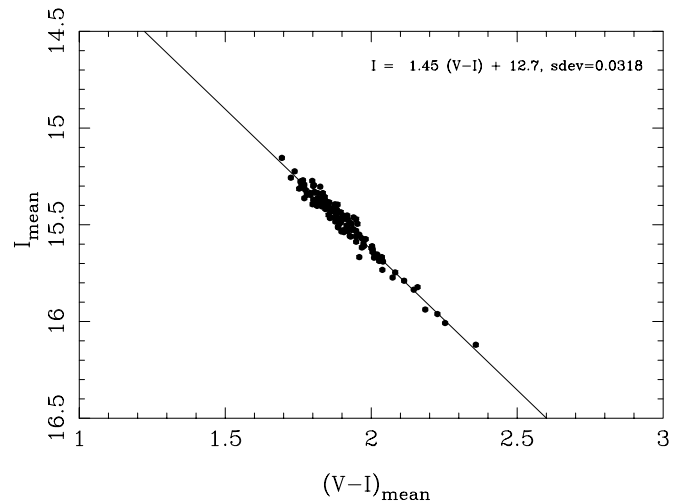


FIG. 12.—Correlation between the mean of $(V-I)$ and I for red clump giants in each subregion. The fitted line is $I = 1.45(V - I) + 12.7$.

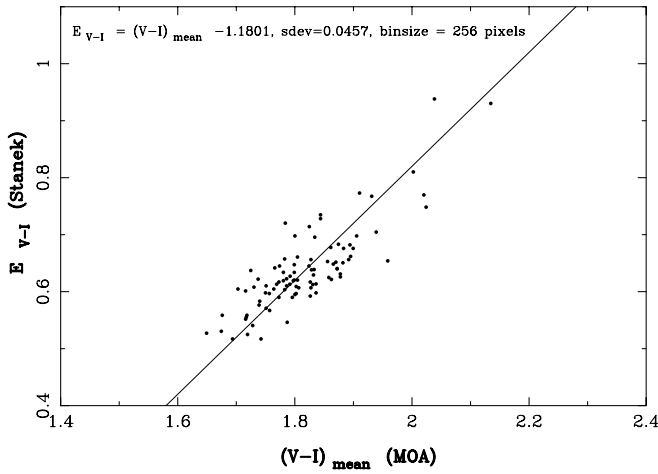


FIG. 13.—Correlation between $(V-I)_{\text{mean}}$ from MOA and E_{V-I} from Stanek (1996) in the overlap regions. The fitted line is $E_{V-I} = (V-I)_{\text{mean}} - 1.18 \pm 0.05$.

$(V-I)$ as follows. We compare $(V-I)_{\text{mean}}$ from our data and the reddening E_{V-I} map (centered on $18^{\text{h}}03^{\text{m}}20^{\text{s}}.9$, $-30^{\circ}02'06''$) calculated by Stanek (1996) in the overlap regions (ngb2-1, ngb2-2, and ngb3-3), where the zero point is based on the determination by Gould, Popowski, & Terndrup (1998) and Alcock et al. (1998). A correlation between $(V-I)_{\text{mean}}$ and E_{V-I} is shown in Figure 13 and equation (18),

$$E_{V-I} = (V-I)_{\text{mean}} - 1.18 \pm 0.05. \quad (18)$$

Using equations (15) and (18), we have made an I -band extinction A_I map from the $(V-I)_{\text{mean}}$ map in our data as shown in Figure 14. The error in A_I is about 0.07 mag. This map is used to make a luminosity function for each region.

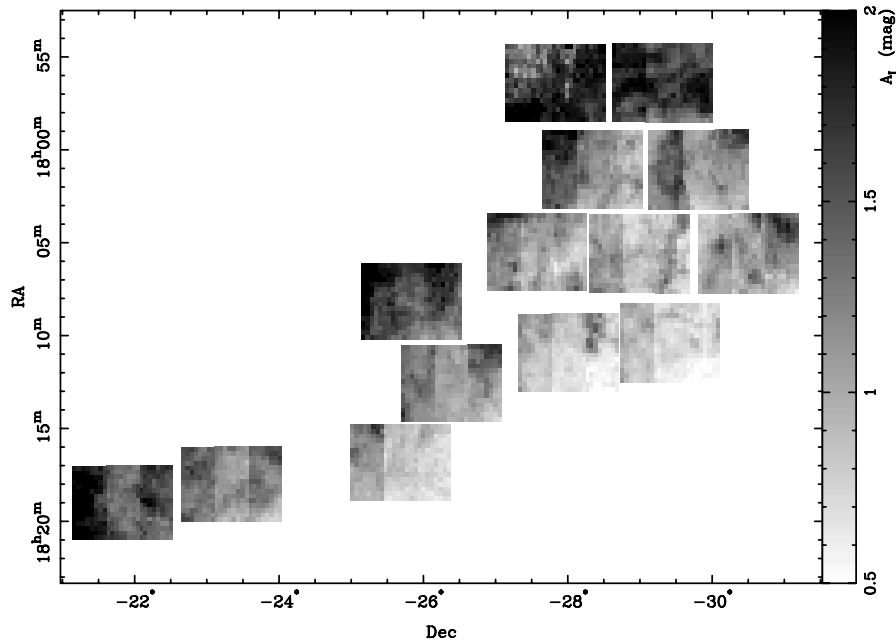


FIG. 14.— I -band extinction A_I map of 14 Galactic bulge fields. The darker regions indicate higher extinction, lighter regions mean lower extinction. We can see the Galactic disk, in which the extinction is high, in the diagonal line from the top right to bottom left.

6. OPTICAL DEPTH

To determine the microlensing optical depth from detected events, we estimate our detection efficiency by Monte Carlo simulations. Here we add artificial microlensed star images to the real subtracted images instead of a full Monte Carlo approach. We then count the number of events that passed the same event selection applied in the real event selection, and estimate the optical depth toward the Galactic bulge.

6.1. Luminosity Functions

To add the artificial microlensing events, we need the luminosity functions (LF) of source stars in GB fields. We use the deepest observations with the *HST* from Holtzman (1998), which measured stars in Baade's window down to $I(\text{F814W}) \sim 24$.

A completeness correction has been applied for the *HST* LF for fainter stars. The bright end of the *HST* LF is poorly defined because of the small field of view ($\sim 5 \text{ arcmin}^2$). Meanwhile, the MOA data have many bright stars because of the wide field of view ($\sim 1.2 \text{ deg}^2$), but are poor for fainter stars, so we combine the *HST* LF and MOA LF at $I = 15\text{--}16$, as shown in Figure 15. Here the MOA LF is made from stars in field ngb2-2 (0.4 deg^2), which includes the *HST* field. The offsets in the photometry of stars in each subregion due to differential extinction are corrected to match that of the *HST* field ($A_I = 0.742 \text{ mag}$). We use the MOA LF for $I < 16$ and the *HST* LF for $I \geq 16$ in this analysis. We use this composite LF for all our GB fields, assuming that the morphology of the LF varies little between the small *HST* field and the large MOA fields.

6.2. Simulation

In each of our 42 subfields ($14 \text{ fields} \times 3 \text{ chips}$), the density of stars, sampling rate, and observational conditions are different. We thus estimate the detection efficiencies

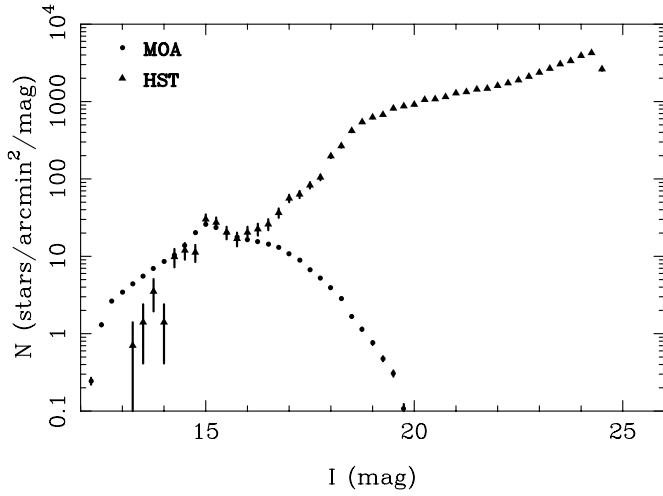


FIG. 15.—Combined luminosity function of Baade’s window from MOA (filled circles) and *HST* (filled triangles). For MOA data the offsets due to differential extinction are corrected to match that of the *HST* field. We use MOA data for $I < 16$ and *HST* data for $I \geq 16$ in this analysis.

individually for each subfield by a Monte Carlo simulation. We generate 429,000 artificial microlensing events in each subfield for this purpose.

A given event has four parameters: u_{\min} , t_E , t_0 , and I_0 . We generated artificial events with the timescale $t_E = 0.3, 0.5, 1, 3, 5, 10, 20, 40, 60, 80, 100, 150,$ and 200 days. For each t_E , we generated events with source extinction-corrected I -band magnitude in the range $12.0 \leq I_0 \leq 22.9$ mag at intervals of 0.1 mag uniformly (the corresponding flux values F_0 were estimated by taking the extinction at each position into account). For each value of t_E and I_0 , 300 events were generated (i.e., 429,000 events for each subfield).

Those parameters that follow a well-known distribution, such as the position (x, y) , the peak time t_0 , and the impact parameter u_{\min} , are selected at random uniformly in the CCD chip ($36 \leq x \leq 2042$ pixels and $5 \leq y \leq 4090$ pixels), in the observation period ($2,451,863.9 \leq \text{JD} \leq 2,451,863.9$), and in $0 < u_{\min} < u_{\text{th}}$, respectively. Here, $u_{\text{th}} = 10^{-0.4(I_0 - I_{\text{th}})} (I_0 \geq I_{\text{th}})$ and $u_{\text{th}} = 1 (I_0 \leq I_{\text{th}})$. We set $I_{\text{th}} = 16$ mag (for ngb1, 4, 5, and 10), 16.5 mag (for ngb2, 3, 6, 8, and 11), and 17 mag (for ngb7, 9, and 12), depending on the mean extinction in their fields. We ensured that the events with $u_{\min} > u_{\text{th}}$ are not detectable in our experiments from former simulations. This u_{th} is introduced to enlarge the statistics for the faint-source events. The slope of $1/u_{\text{th}}$ is roughly consistent with the slope of our combined GB LF, $\psi(I)$, which means the number of generated events is roughly following the LF for faint-source events.

Many other components that are expected to affect the event detection, e.g., bad pixels, seeing, extinction, sample rate, star density, focusing, tracking, sky background, clouds, PSF variation in the focal plane, differential refraction, variable stars, saturated stars, cosmic rays, satellites, asteroids, systematic residuals, and any other unknown systematic noise, are automatically simulated because we use real subtracted images in this simulation.

To generate artificial microlensing events, we add the artificial differential star images on a time series of real subtracted images. The differential stars are made from the

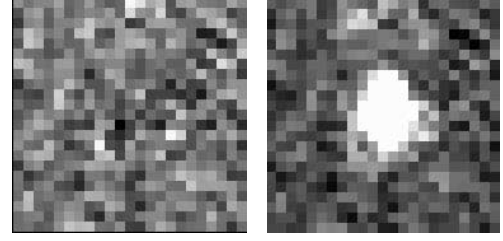


FIG. 16.—Sample of a cut raw subtracted sub-image (23×23 pixels) without (left) and with (right) an artificial event.

local PSF, which was formed by the same procedure outlined in § 3.2, and scaled by the differential flux expressed in equation (14).

In generating the artificial image, the photon noise is taken into account following Poisson statistics, with an additional flux in the current image. The ADU flux of the artificial star in the current image, $F_0 A(t)$ in equation (14), is calculated in the scale of the reference image. Thus, to estimate the photon noise from the additional flux, this additional flux should be transformed to the number of electrons in the current image, given by $F_0 a_0 / G$, where G and a_0 are the gain in ADU/e^- and a scale factor in the kernel, respectively. Then the electron signals are simulated randomly following a Poisson distribution with the mean value of $F_0 a_0 / G$. The resulting simulated random electron signals are rescaled back to the reference image in ADU by multiplying by G/a_0 .

The photon noise from the sky and the blending stars in the current image and reference image are already included in the real subtracted images. Furthermore, the systematic noise from the poor subtraction due to the low S/N is also included. These noise sources depend heavily on the sky condition, seeing, tracking of the telescope, and star density of each frame, so it is complicated to simulate with full artificial images.

We cut out a small sub-image of 23×23 pixels from the subtracted image at a randomly selected position, and put the corresponding differential flux $\Delta F(t)$ onto each sub-image. Figure 16 shows a sample of the cut raw subtracted image (left panel) and the generated artificial differential image (right panel).

For a series of generated artificial images, we apply the same variable object detection process as in § 3.1, and the same PSF photometry as in § 3.2. Saturated pixels ($> 30,000$ ADU) are rejected as in the real analysis. The resulting light curves are stored in the database of artificial events. Sample artificial light curves are shown in Figure 17.

We count the number of artificial events $n(t_E, I_0)$ that passed all criteria for the real event selection for each t_E and I_0 . Then we calculate our detection efficiencies.

6.3. Detection Efficiencies

We show our detection efficiencies as a function of the event timescale, the source magnitude, and the minimum impact parameter.

6.3.1. Detection Efficiency as a Function of Event Timescale

The detection efficiency $\varepsilon_0(t_E, I_0)$ for each sample with t_E and I_0 is given by $\varepsilon_0(t_E, I_0) = n(t_E, I_0)/300$, where $n(t_E, I_0)$

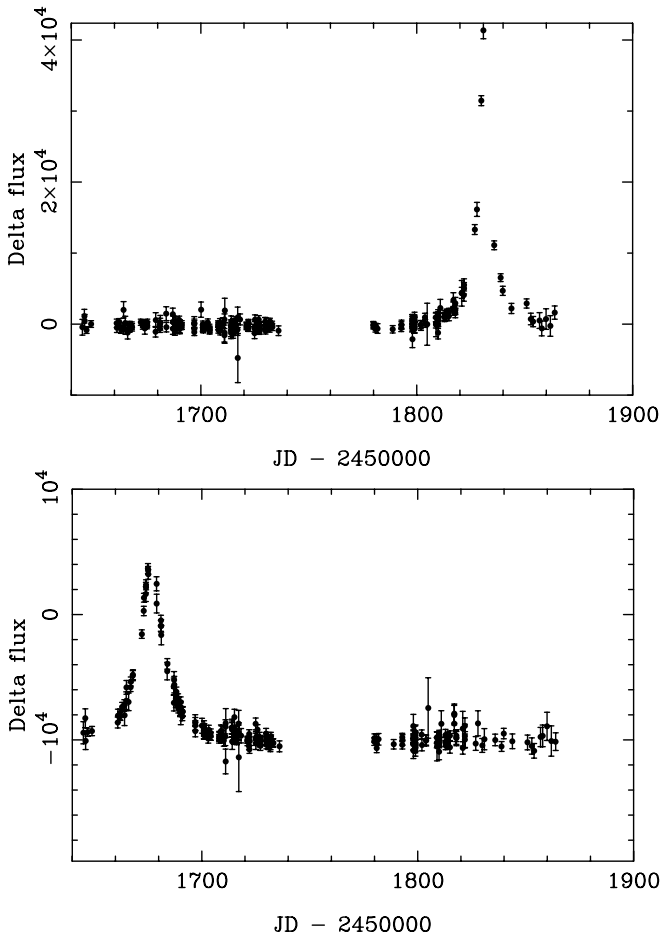


FIG. 17.—Sample light curves of artificial microlensing events with $t_E = 20$ days and $I_0 \sim 17$.

is the number of artificial events that passed our event selections. Then the efficiency $\varepsilon(t_E)$ for t_E is integrated by weighting by the LF $\psi(I)$ as

$$\varepsilon(t_E) = \frac{1}{N_{23}} \int_{I=12}^{I=23} \varepsilon_0(t_E, I) \psi(I) u_{\text{th}} dI, \quad (19)$$

where

$$N_{23} = \int_{I=12}^{I=23} \psi(I) dI. \quad (20)$$

Figure 18 shows one of the resulting detection efficiencies as a function of t_E for bright stars ($I \sim 14$, *dashed line*) and for all possible sources ($I < 23$, *solid line*). Most events with bright source stars whose timescale is longer than 3 days can usually be detected.

On the other hand, the total event detection efficiencies ($I < 23$; Fig. 18, *solid line*) are very low. This is because most source stars are fainter than our observational limiting magnitude of $I \sim 17$. These faint source stars can be detected by microlensing only when they are highly magnified. The possibility that such a high magnification (i.e., small impact parameter u_{min}) event occurs is small. Furthermore, such faint-source events cannot be detected any more for shorter timescale events.

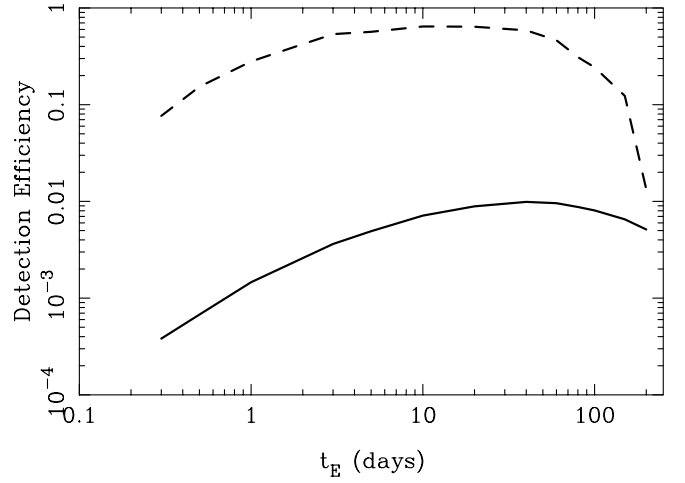


FIG. 18.—MOA detection efficiency as a function of t_E for the ngl-2 subfield for all source stars ($I < 23$, *solid line*) and for bright sources ($I = 14$, *dashed line*). The efficiencies slightly differ for each subfield because of differences in the sampling rate, the star density and the extinction.

6.3.2. Detection Efficiency as a Function of Source Magnitude

We present the detection efficiencies averaged over all subfields as a function of the source I -band magnitude I_0 for various event timescales in Figure 19, where I -band magnitudes are extinction corrected to match those of the *HST* field ($A_I = 0.742$). The efficiencies are very high for brighter source events, as expected. One can see the falloff at the bright end of this efficiency curve due to the saturation of the source star images. The fact that this effect appears in our simulation is one piece of evidence that this simulation is realistic. On the other hand, efficiencies fall off for fainter stars, as expected. The maximum of our detection efficiency is not high, even for bright-source events, because our data have a gap for ~ 40 days due to the malfunctioning of our camera system.

Comparing each of the timescales, the efficiency falls off more significantly for the long-timescale events than for the shorter timescale events at the bright end of these curves. This is because the number of saturated points is large, and

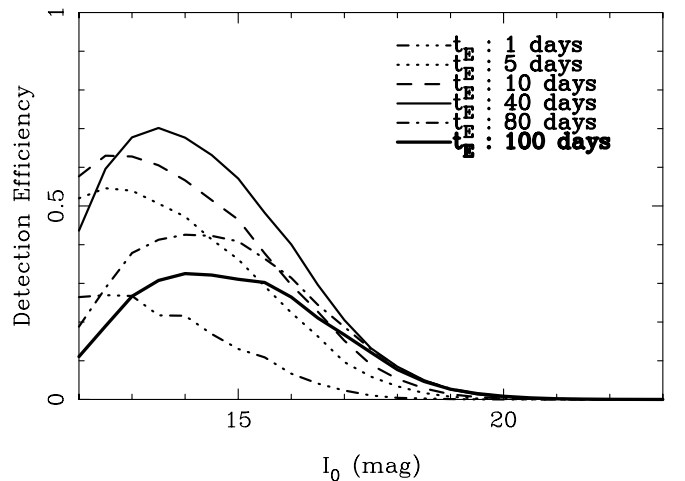


FIG. 19.—MOA detection efficiencies averaged over all subfields as a function of source I -band magnitude I_0 for the various event timescales as indicated in figure.

we required a stable flat baseline to identify the event. In the long-timescale events ($t_E > 50$ days), the stable flat baseline in the light curve is very short. These effects are significant for brighter source and longer timescale events, and vice versa. Meanwhile, at the faint end, the efficiencies are inverted compared to those at the bright end. The duration with a significant excess in the light curve is longer for long-timescale events than for shorter timescale events, which can no longer be detected. We note that there is a small but still nonnegligible efficiency down to $I \sim 22$. This is the main improvement in the analysis by changing from DoPHOT to DIA.

To emphasize this effect, we show the relative expected event rate as a function of I_0 for various event timescales in the top left panel of Figure 20. These are estimated by multiplying Figure 19 by the combined GB LF $\psi(I)$ (Fig. 15), i.e., the integrand of equation (19). The expected source distributions are peaked around $I \sim 19$ and go down to $I \sim 22$, although the observational limiting magnitude of our telescope and camera is $I \sim 17$. This shows the dramatic capability of DIA. In particular, note that this effect is increased by the high sampling rate strategy that we have adopted. Although the sensitivity attained by the MACHO group (Alcock et al. 2000) became 2 mag deeper than their observation limiting magnitude of $V \sim 21$ using DIA, that of

MOA is ~ 5 mag deeper than our observation limiting magnitude of $I \sim 17$. (Of course, this effect also depends on the shape of the luminosity function around the observation limiting magnitude for each experiment.) The longer the timescale is, the fainter the source events that could be detected.

In the top right panel in Figure 20, the observed I -band baseline magnitude I_0 distribution is shown as the histogram, with corresponding expected event rates scaled to match the histogram. Here the observed I_0 is dereddened to match that in the *HST* field. The expected and observed distributions are in good agreement for the observed t_E range ($5 < t_E < 100$ days).

As mentioned in § 4.1.3, many possible microlensing events are rejected by the condition $t_E < 200$ days in cut 3. These events have a significant increase in ΔF , but their parameters could not be well constrained, because the light curve has been measured only around the peak. If the baseline flux is measured by the follow-up observations, t_E could be constrained. If we make a catalog of all variable stars and DNe as we are now doing, or if we observe with two colors, we could easily identify the real microlensing events and issue alerts without the $t_E < 200$ day criterion.

We show the expected event rates without the cut $t_E < 200$ days in the bottom left panel of Figure 20. In this

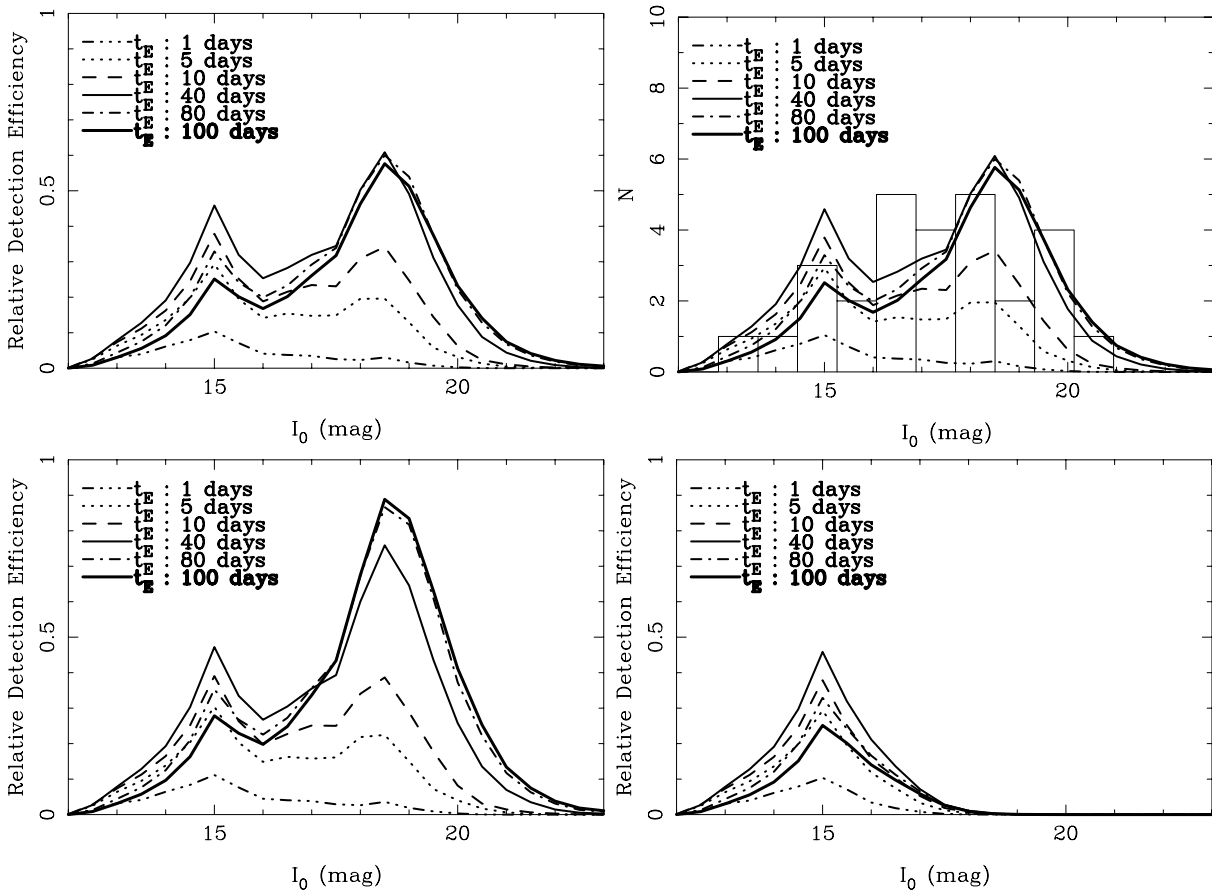


FIG. 20.—Expected relative event rates as a function of the source I -band magnitude I_0 for the various event timescales as indicated in figure. *Top left*: Expected event rates in this analysis. *Top right*: Histogram of the observed baseline magnitude I_0 with corresponding expected event rates scaled to match the histogram. The expected and observed distributions are in good agreement for the observed range of t_E ($5 < t_E < 100$ days). *Bottom left*: Expected event rates without the cut of $t_E < 200$ days in cut 3. A significant increase can be seen for the longer timescale events with the dimmer source stars. *Bottom right*: Expected event rates for the case that the sources are only resolved stars in the reference image, which corresponds to the event rate by DoPHOT-type analysis. This is shown in comparison with that by DIA.

figure we can see a significant increase in the expected event rate for the longer timescale events with the dimmer source stars, which intrinsically should have high amplification. We can see this effect in the minimum impact parameter distribution in § 6.3.3. On the other hand, no significant change can be seen for the short-timescale events, although the duration of the excess in the light curve of these events is as short as that of the long-timescale faint-source events. Thus, the efficiency for the short-timescale events is not affected by this criterion.

To compare these results with the traditional DoPHOT analysis, in which the source star should be resolved in the reference image, we show the same distributions using only the MOA luminosity function (Fig. 15, *filled circles*) as the source luminosity distribution in the bottom right panel of Figure 20. This is not actually the same case as with DoPHOT, because the DIA can improve the photometric accuracy, even for stars resolved in the reference image. Furthermore, there are many faint-source events that are blended by bright resolved stars. These effects will cancel each other. In any case, they are relatively small effects when compared to the differences in the DIA and DoPHOT analysis, so this distribution should not be much different from the actual one and should make a meaningful comparison. In this figure, the difference between DoPHOT (*bottom right*) and DIA (*top left*) is clear. The peak of this distribution is at $I \sim 15$, which corresponds to the second peak in the top left panel of Figure 20. The DIA method increases the number of events by more than a factor of 2. In particular, we can detect many events in which the source stars are fainter than the observational limiting magnitude by using DIA.

6.3.3. Minimum Impact Parameter Distribution.

Because of the simple geometry of microlensing, the probability distribution of the minimum impact parameter u_{\min} is uniform. In actual experiments, however, the distribution of the detection efficiency in u_{\min} , i.e., the expected event rate distribution, is biased toward smaller u_{\min} , because the high amplification makes it easier to detect the event.

This effect can be seen in Figure 21, which shows our observed u_{\min} distribution (*histogram*) and the estimated

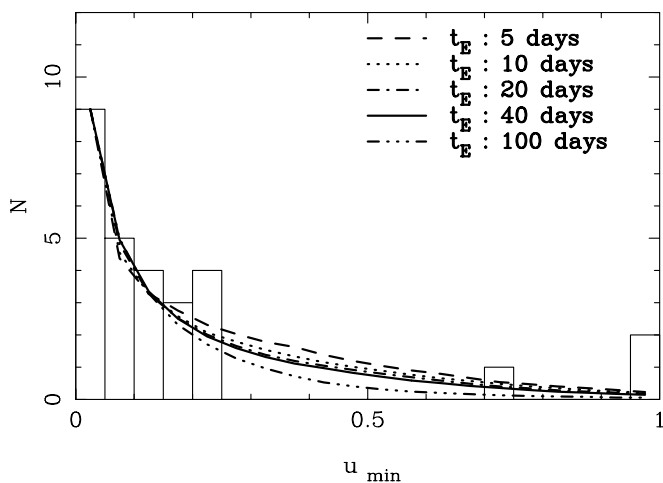


FIG. 21.—Observed u_{\min} distribution (*histogram*) and the estimated distributions (*lines*) scaled to match the histogram at $u_{\min} = 0.05$ for various timescales as indicated in the figure.

one in the simulation (*lines*) for various timescales that are scaled to match the histogram at $u_{\min} = 0.05$. Here the lines are the mean efficiencies for all our fields. These observed and estimated distributions are in good agreement for the range of the observed timescales (between 5 and 100 days).

In this figure we can see that half of the detected events have a small minimum impact parameter ($u_{\min} < 0.1$), although the fraction of events with $u < 0.1$ is only 10% in the DoPHOT analysis (Alcock et al. 1997a) and 30% in the recent DIA analysis (Alcock et al. 2000) by the MACHO group. This is because our sampling rate is higher (5–6 times per day) than theirs (once per day).

If events that fail by the criterion $t_E < 200$ days are included as mentioned in the previous section, then 5%–15% more high-magnification events would be expected. Figure 22 shows the estimated u_{\min} distribution for the typical timescale of $t_E = 40$ days without (*solid line*) and with (*dashed line*) this $t_E < 200$ day cut. We also show the same distribution with the $t_E < 200$ day cut for brighter source stars ($I < 17$), which correspond to the DoPHOT analysis. From this figure, it is clear that our analysis with DIA (*solid line*) can detect the high-magnification events more efficiently than a DoPHOT-type analysis (*dot-dashed line*). Furthermore, it will be possible to detect more ($\sim 10\%$) high-magnification events without the $t_E < 200$ day cut (*dashed line*) in the near future.

6.4. Optical Depth

Here we estimate the optical depth toward the Galactic bulge by using the observed events and our detection efficiencies.

6.4.1. Optical Depth Estimation

The optical depth τ is defined as the probability that any given star is microlensed with impact parameter $u_{\min} \leq 1$ at any given time. The τ can be estimated by

$$\tau = \frac{\pi}{2N_s T_o} \sum_i \frac{t_{E,i}}{\varepsilon(t_{E,i})} \quad (21)$$

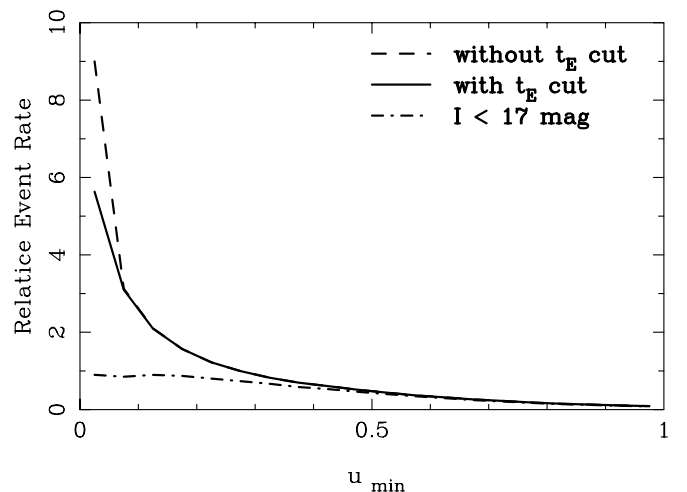


FIG. 22.—Estimated u_{\min} distribution for the typical timescale of $t_E = 40$ days with (*solid line*) and without (*dashed line*) the $t_E < 200$ day cut. Also shown for comparison is the same distribution with a $t_E < 200$ day cut for the bright source star ($I < 17$) events (*dot-dashed line*), which is scaled to match the others at $u_{\min} = 1$.

where N_s is the total number of source stars in the observation fields, T_o is the duration of observation of this analysis in days, $t_{E,i}$ is the event timescale for the i th event, and $\varepsilon(t_{E,i})$ is the detection efficiency for a given timescale.

We estimate N_s for $I < 23$ by using the number of bright stars ($I < 15$, extinction corrected) whose observation efficiency is nearly 100%, and our combined LF. This is because our detection efficiencies have been estimated by taking all stars with $I < 23$ into account.

We estimate the optical depth by using the observed timescales with $N_s \sim 250$ million stars ($I < 23$), $T_o = 219$ days for ngb1 ~ 12 . We do not include fields ngb13 and 14 in this analysis because these two fields are far from Baade's window. For events with timescales within $0.3 < t_E < 200$ days, we estimate the optical depth as

$$\tau = 2.63_{-0.58}^{+0.72} \times 10^{-6}, \quad (22)$$

where the lower and upper limit of this value are estimated by a Monte Carlo simulation following Alcock et al. (1997a, 1997b, 2000) and assuming a Poisson distribution. We have simulated 100,000 "experiments" for each N_{exp} , which is the number of expected events, and chosen at 0.5 intervals between 0 and 60 events. In each experiment the number of detected events N is selected by following the Poisson statistics with the mean value of N_{exp} . For each simulated event, we randomly selected one of our observed event timescales. We have estimated the probability $P(\tau(N) > \tau_{\text{obs}})$ that the optical depth $\tau(N)$ in each simulated experiment is larger than the observed one τ_{obs} , and the mean optical depth $\langle \tau(N_{\text{exp}}) \rangle$ for each distribution with N_{exp} . We show this probability distribution in Figure 23, from which we have estimated the 1σ confidence limit of the optical depth.

This estimate gives errors which are a lower limit, because errors in t_E are ignored. We found a large uncertainty and systematic bias in the "INPUT" t_E (hereafter $t_{E,\text{in}}$) and measured "OUTPUT" t_E (hereafter $t_{E,\text{out}}$) in our artificial events generated in § 6.2. We show the relation between $t_{E,\text{in}}$ and the mean value of $t_{E,\text{out}}$ for various source magnitude in Figure 24. As we can see in this figure, the measured $t_{E,\text{out}}$ tend to be larger in small $t_{E,\text{in}}$ and smaller in large $t_{E,\text{in}}$. This

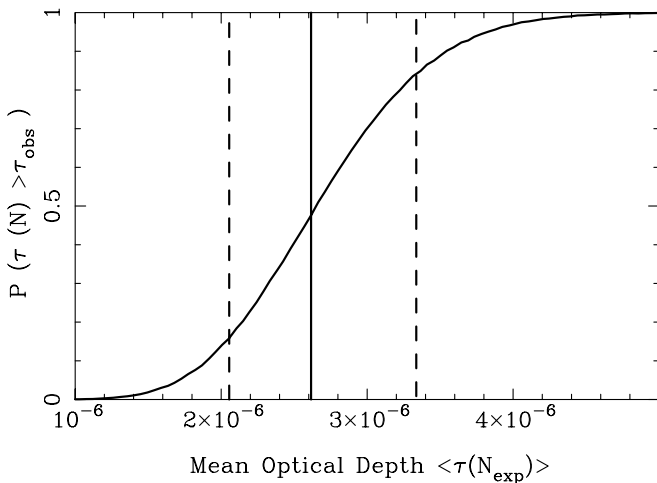


FIG. 23.—Probability $P(\tau(N) > \tau_{\text{obs}})$ that the optical depth $\tau(N)$ in each simulated experiment is larger than the observed one τ_{obs} as a function of the mean optical depth $\langle \tau(N_{\text{exp}}) \rangle$ of experiments in which an expected event number is N_{exp} . 1σ confidence limits (dashed line) and the observed optical depth τ_{obs} (solid line) are also presented.

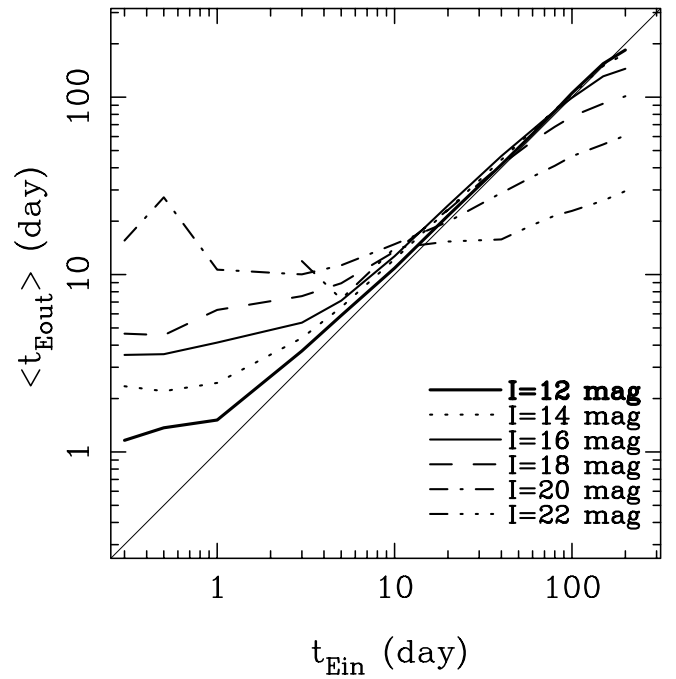


FIG. 24.—Relation between $t_{E,\text{in}}$ and the mean value of $t_{E,\text{out}}$ for various source I -band magnitude as indicated in the figure. The mean $\langle t_{E,\text{out}} \rangle$ are taken over the events between each indicated I magnitude and $I + 1$ mag. We have no detection in $t_{E,\text{in}} \leq 1$ day for $I = 22$.

is because we cut events with $t_{E,\text{in}}$ outside $0.3 < t_E < 200$ days. This effect is larger particularly for fainter source events because of their large scatter in $t_{E,\text{out}}$. However, for relatively brighter source events with $10 \leq t_{E,\text{in}} \leq 60$ days, there is only a quite small bias that $t_{E,\text{out}}$ tend to be slightly larger.

We carried out a full Monte Carlo simulation to measure the error in the optical depth and bias using these artificial events. We used lists of measured OUTPUT $t_{E,\text{out}}$ of artificial events for each INPUT value of $t_{E,\text{in}}$ and I_0 , which consist of about 100,000 artificial events for each subfield.

The number of expected events for each I_0 is proportional to $\sim \varepsilon_0(t_E, I_0) \psi(I_0) u_{\text{th}}$, i.e., the integrand of equation (19). Following this number of expected events for each I_0 , we picked OUTPUT $t_{E,\text{out}}$ randomly from the lists and put them into the expected OUTPUT $t_{E,\text{out}}$ distribution $D_{\text{out}}(t_{E,\text{in}})$ until the total number of events become $\sim 40,000$ for each INPUT $t_{E,\text{in}}$. We show an example of this distribution for $t_{E,\text{in}} = 40$ days, i.e., $D_{\text{out}}(40)$, in Figure 25.

We used our observed t_E distribution as the INPUT $t_{E,\text{in}}$ distribution for the simulation. We do not have any artificial events with exactly the same t_E as that of observed events, so we linked each event to artificial events that have a similar INPUT $t_{E,\text{in}}$ value. For example, event ngb1-2-2745 ($t_E = 41.3$ days) was linked to artificial events with $t_{E,\text{in}} = 40$ days, and ngb1-2-5076 ($t_E = 51.8$ days) was linked to artificial events with $t_{E,\text{in}} = 40$ and 60 days with 50% probability. The linked INPUT $t_{E,\text{in}}$ of artificial events were listed in the INPUT $t_{E,\text{in}}$ distribution D_{in} .

We performed the same simulation as above using D_{in} and $D_{\text{out}}(t_{E,\text{in}})$, i.e., we simulated 100,000 experiments for each N_{exp} . For each simulated event, we randomly select one $t_{E,\text{in}}$ from D_{in} and choose one $t_{E,\text{out}}$ from the corresponding OUTPUT distribution $D_{\text{out}}(t_{E,\text{in}})$ at random.

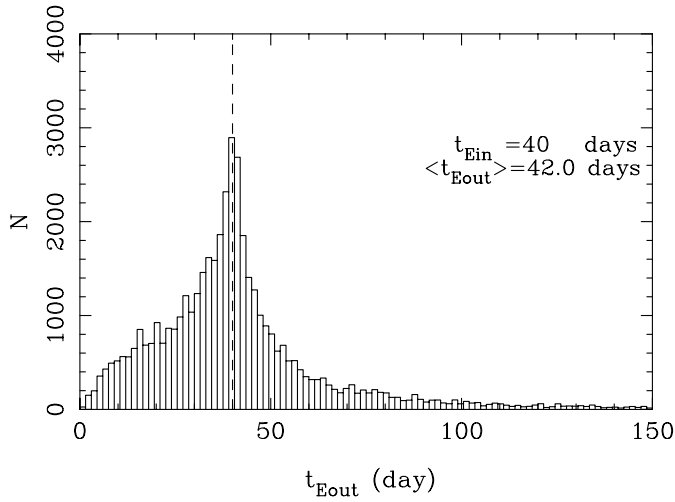


FIG. 25.—Example of the expected OUTPUT $t_{E,out}$ distribution for $t_{E,in} = 40$ days (vertical dashed line), i.e., $D_{out}(40)$. The mean $\langle t_{E,out} \rangle$ is 42 days in this case.

Then we measure the INPUT and OUTPUT optical depths (τ_{in} and τ_{out}) from $t_{E,in}$ and $t_{E,out}$, respectively, for each experiment. We ensured that the τ_{in} in the case of $N_{exp} = 28$ is the same as the observed value, $\tau_{obs} = 2.63 \times 10^{-6}$. This is expected because D_{in} was made from our observed t_E distribution.

We plot the difference between the mean values of τ_{in} and τ_{out} in Figure 26. We can see the existence of the small bias between them. The τ_{out} tend to be slightly larger than τ_{in} . From this relation, the real optical depth is estimated to be $\tau = 2.59 \times 10^{-6}$ from the observed optical depth of $\tau_{obs} = 2.63 \times 10^{-6}$.

To estimate the error in this optical depth, we have used the same method as above but with τ_{out} instead of τ_{in} . The standard deviation of τ_{out} is $\sim 16\%$ larger than that of τ_{in} for each N_{exp} . We have estimated the probability

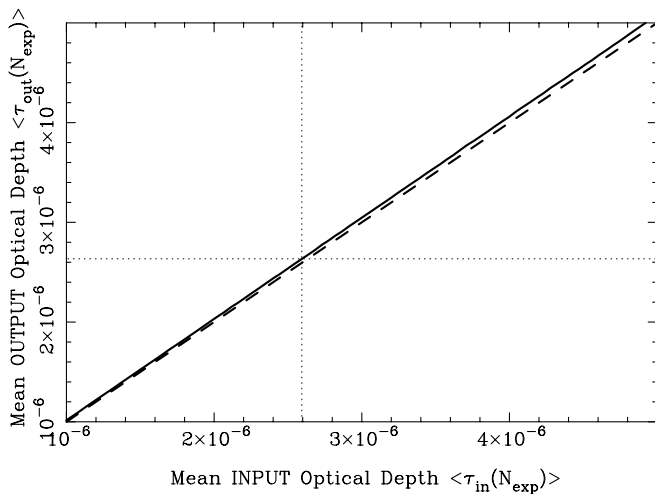


FIG. 26.—Relation between mean optical depth of OUTPUT ($\langle \tau_{out}(N_{exp}) \rangle$) and INPUT ($\langle \tau_{in}(N_{exp}) \rangle$) (solid line). Dashed line represents $\langle \tau_{out}(N_{exp}) \rangle = \langle \tau_{in}(N_{exp}) \rangle$. The horizontal and vertical dotted line indicate observed ($\tau_{obs} = 2.63 \times 10^{-6}$) and estimated ($\tau = 2.59 \times 10^{-6}$) optical depths, respectively.

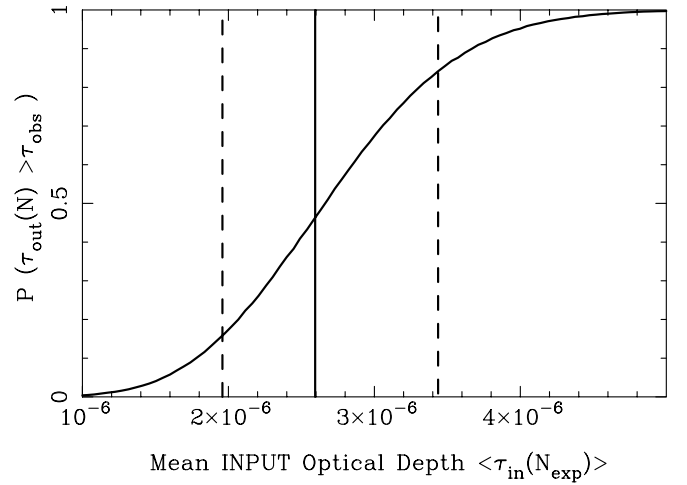


FIG. 27.—Probability $P(\tau_{out}(N) > \tau_{obs})$ that the OUTPUT optical depth $\tau_{out}(N)$ in each simulated experiment is larger than the observed one τ_{obs} as a function of the mean INPUT optical depth $\langle \tau_{in}(N_{exp}) \rangle$ of experiments in which an expected event number is N_{exp} . 1 σ confidence limits (dashed line) and the estimated real optical depth τ (solid line) are also presented.

$P(\tau_{out}(N) > \tau_{obs})$ that the optical depth $\tau_{out}(N)$ in each simulated experiment is larger than the observed one τ_{obs} , and the mean INPUT optical depth $\langle \tau_{in}(N_{exp}) \rangle$ for each distribution with N_{exp} . We show this probability distribution in Figure 27. From this we have estimated the 1 σ confidence limit of the INPUT optical depth τ_{in} . These 1 σ errors are about 15% larger than errors from the method with Poisson statistics only. The resulting optical depth and errors are

$$\tau = 2.59_{-0.64}^{+0.84} \times 10^{-6}. \quad (23)$$

This τ is mostly due to disk and bulge (bar) stars. The optical depth in the direction of the Galactic bulge due to halo objects of any kind is only $\sim 0.13 \times 10^{-6}$ (Griest et al. 1991). This τ is underestimated because some fraction of the source stars are foreground disk stars, for which the optical depth is considerably lower.

6.4.2. Disk Contribution

The optical depth estimated in the previous section is underestimated. In the number of stars in our fields, N_s , some fraction of the stars are probably foreground Galactic disk stars. The optical depth for the disk source stars (so-called disk-disk events) is quite small. There are also background disk stars which would have a higher optical depth, but our line of sight toward the bulge is several hundred parsecs out of the Galactic plane on the far side of the bulge. Most of the disk contamination is therefore from foreground disk stars. The fraction of disk stars in our fields is rather uncertain.

We estimate the fraction of disk stars out of all stars, f_{disk} , in our fields. We use the nonrotating triaxial bar models with a bar inclination angle of $\theta = 20^\circ$, whose density profile as a function of the distance D from the Sun is given by (Han & Gould 1995a; Alcock et al. 2000)

$$\rho_b(w) = \frac{M}{20.65abc} \exp\left(-\frac{w^2}{2}\right), \quad (24)$$

$$w^4 = \left[\left(\frac{x'}{a} \right)^2 + \left(\frac{y'}{b} \right)^2 \right]^2 + \left(\frac{z}{c} \right)^4. \quad (25)$$

Here the coordinates (x', y') are measured along the longest axis and another axis of the bar in the Galactic plane. The x' -axis is aligned at an angle θ from the line of sight to the Galactic center from the Sun, with the near side of the bar in the positive- l quadrant. The z -axis is as usual the height above the Galactic plane. These Galactocentric coordinates (x', y', z) are given by $x' = R_0 \cos \theta - D \cos b \cos(l + \theta)$, $y' = R_0 \sin \theta - D \cos b \sin(l + \theta)$, and $z = D \sin b$, where R_0 is the distance to the Galactic center from the Sun, taken to 8.5 kpc. Here $a = 1580$ pc, $b = 620$ pc, and $c = 430$ pc define the bar scale lengths, and $M = 1.8 \times 10^{10} M_\odot$ is the total bar mass.

We use the standard double-exponential disk whose density profile is given by (Han & Gould 1995a; Alcock et al. 2000)

$$\rho_d = \rho_{d0} \exp\left(\frac{-|z|}{h_z} - \frac{R - R_0}{R_d}\right), \quad (26)$$

where $R = R_0^2 + D^2 \cos^2 b - 2R_0 D \cos b \cos l$ and $z = D \sin b$ are the disk cylindrical Galactocentric coordinates, D is the distance from the Sun, and (l, b) are the Galactic latitude and longitude. Here $h_z = 325$ kpc and $R_d = 3.5$ kpc are the disk scale height and length, and $\rho_{d0} = 0.06 M_\odot \text{pc}^{-3}$ is the density constant chosen to match the density in the solar neighborhood.

These models give optical depths toward Baade's window $(l, b) = (1^\circ, -3^\circ 9')$ of 1.2×10^{-6} from the bar and 0.6×10^{-6} from the disk. By using these density models and Kiraga & Paczyński (1994)'s luminosity function with $\beta = -1$ (see § 7), f_{disk} is estimated as $\sim 23\%$. This value is consistent with the value used by the MACHO group of $f_{\text{disk}} \sim 20\%$ (Alcock et al. 1997a) and $f_{\text{disk}} \sim 25\%$ (Alcock et al. 2000), where most of our GB fields are overlapping with their fields. This gives

$$\tau_{\text{bulge}} = 3.36_{-0.81}^{+1.11} \times 10^{-6} \left(\frac{0.77}{1 - f_{\text{disk}}} \right). \quad (27)$$

This optical depth is consistent with the previous observations of $3.3_{-1.2}^{+1.2} \times 10^{-6}$ from nine events by DoPHOT analysis (Udalski et al. 1994), $3.9_{-1.2}^{+1.8} \times 10^{-6}$ from 13 events in the clump giant subsample by DoPHOT (Alcock et al. 1997a), and $3.23_{-0.50}^{+0.52} \times 10^{-6}$ from 99 events by DIA (Alcock et al. 2000), while slightly higher than the $2.0_{-0.4}^{+0.4} \times 10^{-6}$ from Popowski et al. (2001) and $2.23_{-0.35}^{+0.38} \times 10^{-6}$ from Popowski (2002).

This measured optical depth must be regarded as a lower limit of the true value because our observations are only sensitive to the events with $0.3 < t_E < 200$ days. Nevertheless, this value is still higher than those predicted by most Galactic models, whose mass and inclination of the bar are consistent with other observations. We note that our observed optical depth values are averaged over 16 deg^2 (12 fields) around Baade's window $(l, b) = (1^\circ, -3^\circ 9')$, while in most calculations the optical depth is estimated exactly toward Baade's window. However, we ignore this difference in this paper, since it is negligible in most models. Even the smallest inclination angle and a large bar mass have been reported to be insufficient to produce an optical depth greater than $\sim 2.5 \times 10^{-6}$ (Peale 1998).

7. TIMESCALE DISTRIBUTION

The observed timescale distribution depends on the mass function and the velocity dispersion of the lens. To make meaningful models of Galactic structure, both the optical depth and the timescale distribution should be consistent with the observations. Peale (1998) and Mera, Chabrier, & Schaeffer (1998) show that it is difficult to reproduce the observed timescale distribution of Alcock et al. (1997a) with the existing Galactic models. We show our observed timescale distribution in Figure 28.

For comparison, in Figure 28 we also plot the expected timescale distribution for a fixed bar (eq. [24]) and disk (eq. [26]) density model with various mass functions. These distributions are corrected by our detection efficiencies and normalized to the number of observed events. Where we followed the method of Kiraga & Paczyński (1994), Han & Gould (1995a), and Alcock et al. (2000), assuming the mean velocity \bar{v} and variance σ of the components in the bar and disk for each direction (y and z) as $(\bar{v}_{\text{bar},y}, \bar{v}_{\text{bar},z}) = (0, 0)$ and $(\sigma_{\text{bar},y}, \sigma_{\text{bar},z}) = (110, 110)$ for the bar lens and source, $(\bar{v}_{\text{disk},y}, \bar{v}_{\text{disk},z}) = (220, 0)$ and $(\sigma_{\text{disk},y}, \sigma_{\text{disk},z}) = (30, 30)$ for the disk lens, and $(\bar{v}_{o,y}, \bar{v}_{o,z}) = (220, 0)$, $(\sigma_{o,y}, \sigma_{o,z}) = (0, 0)$ for the observer in km s^{-1} (Han & Gould 1995a; Alcock et al. 2000). For these bar and disk models, we evaluate timescale distributions toward Baade's window with the following five mass functions: (i) the Scalo (1986) present-day mass function (PDMF); a δ -function at (ii) $M = 0.1 M_\odot$ and (iii) $M = 1.0 M_\odot$; and the power-law $\phi(M) \propto M^{-\alpha}$ with (iv) $\alpha = 2.3$ and low-mass end $M_l = 0.1 M_\odot$, and (v) $\alpha = 2.0$ and $M_l = 0.01 M_\odot$, where mass function (v) represents the brown-dwarf-rich mass function (Alcock et al. 1997a).

The timescale of detected events is distributed in the range $5 < t_E < 100$ days and centered around $t_E \sim 30$ days. This feature is consistent with that from the MACHO group (Alcock et al. 2000), although their distribution is slightly sharper around the mean than ours. The distribution of

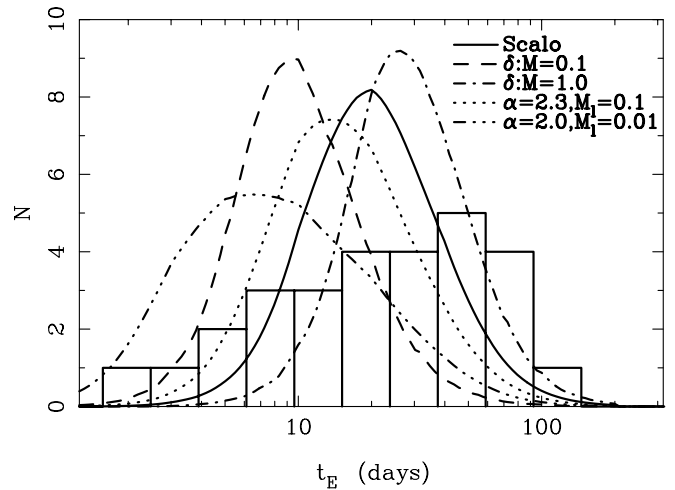


FIG. 28.—Histograms of the event timescale t_E distribution for 28 observed events with expected timescale distributions, normalized to the observed number of events, for a fixed bar and disk density model and for various mass functions. The solid line indicates Scalo (1986)'s PDMF; the dashed and dot-dashed lines indicate δ function at $M = 0.1$ and $1.0 M_\odot$ respectively; the dotted and triple-dot-dashed lines show the power law with $\alpha = 2.3$, $M_l = 0.1$ and $\alpha = 2.0$, $M_l = 0.01$, where the latter represents the brown dwarf rich mass function.

Alcock et al. (2000) is well fitted by the timescale distribution expected from the Scalo (1986) PDMF except for some fraction of long-timescale events, although those models do not explain the large observed optical depth. For our distribution in Figure 28, the Scalo (1986) PDMF also seems to be more reasonable than the others. Although our detection efficiency is sufficiently high for the short-timescale events ($t_E \sim 0.3$ days) because of our frequent sampling (5–6 times per day), there are only two short-timescale events ($t_E < 4$ days). The timescale distribution traces the mass distribution; t_E for the most common events is $\sim 7(M/0.1 M_\odot)^{1/2}$ days for both bulge and disk lenses (Han & Gould 1995a). The number of observed short events is much smaller than that expected from the brown dwarf rich mass function (ν), which is consistent with Alcock et al. (2000). However, this topic is quite complicated. The measurement of t_E has large uncertainty in itself, and its distribution depends on the unknown kinematics of the sources and lenses. A detailed analysis of this topic is beyond the scope of the present study. The identification of brown dwarfs may be possible only with larger statistics of higher S/N events in the future.

We can also see some fraction of long-timescale events ($t_E > 70$ days) as reported in Alcock et al. (2000), which cannot be reproduced with the Scalo (1986) mass function (i) and contemporary Galactic models (Han & Gould 1996). Such long-timescale events could be produced when the lenses are heavy, moving at low transverse velocity, or in the middle of the line from observer to source. If both the lens and source are in the disk, so-called disk-disk lensing, then the timescale would be long. The probability of this is constrained by star counts, and it is very small. There might be some unknown population of dynamically cold or massive dark objects, such as white dwarfs or neutron stars, in the Galactic disk or bulge. Further discussion of this can be found in Alcock et al. (2000).

We show our observed timescale distribution, corrected by the detection efficiency, i.e., the expected true t_E distribution, in Figure 29. This distribution is similar to that of Alcock et al. (2000), except for the short-timescale events. Although their distribution is sharply truncated at $t_E \sim 4$ days except for one short event with $t_E = 1.4$ days, our distribution is flat to 2 days. However, this difference is not significant because these shorter two bins are based on only two events, and the amount is still small.

The contribution to the total optical depth of the observed timescale distribution is given in Figure 30. The contributions of the short-timescale events to the total optical depth are quite small. In any case, we need more observations to investigate the mass function and Galactic structure in more detail.

8. DISCUSSION AND CONCLUSION

We have reanalyzed the sample of subtracted images that were derived from the real-time DIA of GB observations obtained by MOA during 2000 (Bond et al. 2001). In this analysis we have found 28 microlensing event candidates in our 12 GB fields. The DIA is more suitable than DoPHOT analysis for our purpose, since the former method can detect the luminosity variation at any position, even where no star was previously identified.

We have used a Monte Carlo simulation to estimate our event detection efficiencies. By using these efficiencies and timescales of our 28 detected events, we have estimated the

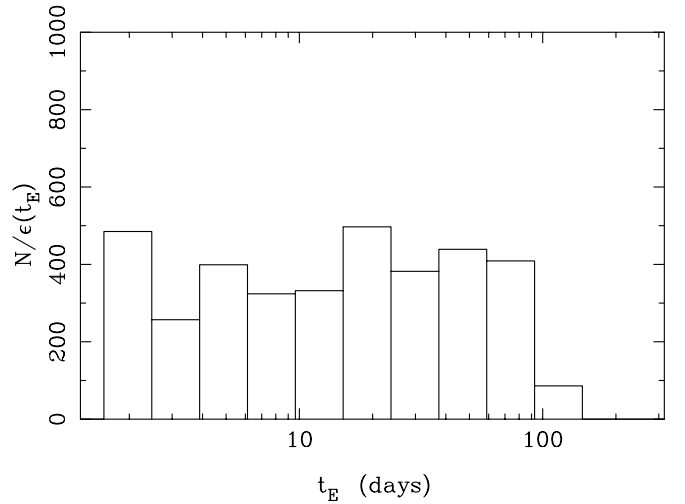


FIG. 29.—Histograms of the observed t_E distribution, corrected for the detection efficiency.

optical depth toward the GB for events with timescales within the range $0.3 < t_E < 200$ days as $\tau_{0.3}^{200} = 2.63_{-0.58}^{+0.72} \times 10^{-6}$, where the statistical uncertainty of the optical depth has been estimated by Monte Carlo simulation only using the Poisson statistics. This τ is overestimated and these errors in τ are underestimated. We found the systematic bias and large uncertainty in the OUTPUT $t_{E,\text{out}}$ in our simulation. By taking this bias and uncertainty in $t_{E,\text{out}}$ into account, we get

$$\tau_{0.3}^{200} = 2.59_{-0.64}^{+0.84} \times 10^{-6}.$$

The GB microlensing optical depth, in which the disk source stars component ($f_{\text{disk}} = 23\%$) is taken into account, is given by

$$\tau_{\text{bulge}} = 3.36_{-0.81}^{+1.11} \times 10^{-6} \left(\frac{0.77}{1 - f_{\text{disk}}} \right).$$

This value is consistent with the previous observations of

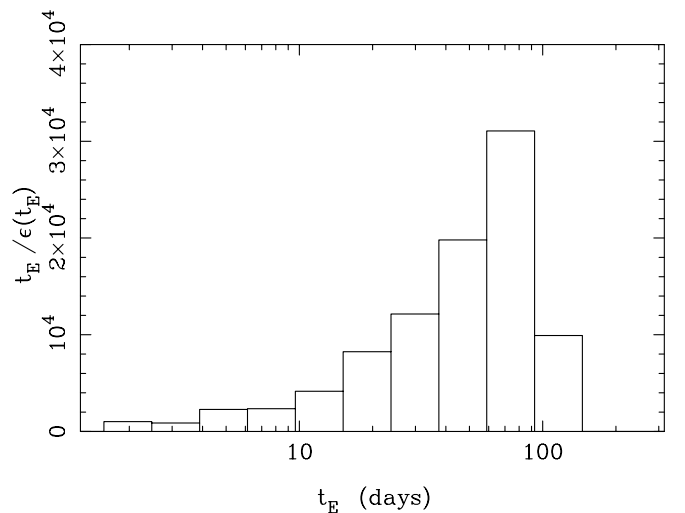


FIG. 30.—Distribution of the contribution to the total optical depth [$t_E/\epsilon(t_E)$] of the observed event t_E . The contribution of the short-timescale events to the optical depth is quite small.

$3.3_{-1.2}^{+1.2} \times 10^{-6}$ from nine events by DoPHOT analysis (Udalski et al. 1994), $3.9_{-1.2}^{+0.9} \times 10^{-6}$ from 13 events in a clump giant subsample by DoPHOT (Alcock et al. 1997a), and $3.23_{+0.52}^{-0.50} \times 10^{-6}$ from 99 events by DIA (Alcock et al. 2000), while slightly higher than the $2.0_{-0.4}^{+0.4} \times 10^{-6}$ from Popowski et al. (2001) and $2.23_{-0.35}^{+0.38} \times 10^{-6}$ from Popowski (2002).

This observed τ must be regarded as a lower limit of the true value, since our observations are only sensitive to events with $0.3 < t_E < 200$ days. Nevertheless, this value is still higher than those predicted by most Galactic models, whose mass and inclination of the bar are consistent with other observations. Even the smallest inclination angle and a large bar mass could not reproduce τ greater than $\sim 2.5 \times 10^{-6}$ (Peale 1998). In Evans & Belokurov (2002), Freudenreich's model can reproduce the high optical depths toward the GB, $\sim 2.5 \times 10^{-6}$, which is about the 1σ level of our estimate.

The smallest inclination produces the largest optical depth. However, the bar inclination has been reported to be in a wide range between 10° and 45° , summarized in Table 7 in Alcock et al. (2000). The optical depth also depends on the mass of the bulge or bar. However, various observations provide conflicting values of $M_{\text{bulge|bar}} = 0.7\text{--}2.8 \times 10^{10} M_\odot$ (Zhao & Mao 1996; Dwek et al. 1995; Holtzman 1998; Han & Gould 1995b; Blum 1995). Very small inclinations ($\theta = 11^\circ$ with $M_{\text{bar}} = 2.0 \times 10^{10} M_\odot$ [Zhao & Mao 1996] and $\theta = 12^\circ$ with $M_{\text{bar}} = 2.5 \times 10^{10} M_\odot$ [Gyuk & Crots 1999]) or a very heavy mass ($\sim 3.6 \times 10^{10} M_\odot$ with $\theta = 20^\circ$; Gyuk & Crots 1999) are required to account for the observed optical depth in this analysis and in Alcock et al. (2000). Binney & Evans (2001) estimate the minimum total mass in baryonic matter within the Solar circle to be greater than $\sim 3.9 \times 10^{10} M_\odot$ from $\tau = 2.0 \times 10^{-6}$, and such a high baryonic contribution is consistent with implications from hydrodynamical modeling and the pattern speed of the Galactic bar.

Such a high mass would imply low halo MACHO fractions (Gates, Gyuk, & Turner 1996). A massive bulge puts tight constraints on the contribution of the disk to the rotation curve at small radii. A small disk, however, leaves more room for the halo. Since microlensing results toward the LMC fix the MACHO content in the halo, a massive halo implies a smaller MACHO fraction.

The uncertainties in the Galactic bar orientation, the bar mass, and the stellar mass function are still large, so the optical depth we have derived might yet be explained by other models. Further discussion can be found in Alcock et al. (2000).

We show our observed timescale distribution, which is not biased by blending. Although our statistics are smaller, this seems to be consistent with the one previously presented by the MACHO group (Alcock et al. 2000). The number of short-timescale events is quite small, in spite of our high detection efficiency for events down to $t_E \sim 0.3$ days.

A significant number of long-timescale ($t_E > 70$ days) events have been detected, as reported previously by the MACHO group (Alcock et al. 2000). These could not be explained by any current Galactic model (Han & Gould 1996). These might be a heavier remnant component, such as white dwarfs, or some dynamically cold component. Either way, we need more observations to investigate the mass function and Galactic structure in greater detail.

We have shown how efficiently MOA can detect the high-magnification events, in which the probability of detecting extrasolar planets is high, and find that 50%–60% of all detected events have high magnification ($u_{\text{min}} < 0.1$). This fraction is much higher than the 10% from DoPHOT analysis (Alcock et al. 1997a) and 30% from recent DIA analysis (Alcock et al. 2000) by the MACHO group. This is because our sampling rate is higher (5–6 times per day) than theirs. These results support our belief that high-frequency observations and analysis using DIA, which MOA is currently carrying out, can detect high-magnification microlensing events very efficiently, even with a small telescope.

We acknowledge J. Holtzman, K. Stanek, the MACHO collaboration, and the OGLE collaboration for making their data publicly available. We would like to thank B. Paczyński, S. Mao, and M. Smith for carefully reading the manuscript and comments. We acknowledge A. Drake for helpful suggestions. We are also thankful to the referee for helpful comments. Financial support from the Royal Society of New Zealand's Marsden Fund, Grant-in-Aid for Scientific Research A, B, and the database of the Japanese Ministry of Education and Science are gratefully acknowledged. T. S. acknowledges financial support from the Nishina Memorial Foundation.

REFERENCES

- Alard, C. 2000, *A&AS*, 144, 363
 Alard, C., & Lupton, R. H. 1998, *ApJ*, 503, 325
 Alcock, C., et al. 1997a, *ApJ*, 479, 119
 ———. 1997b, *ApJ*, 486, 697
 ———. 1998, *ApJ*, 494, 396
 ———. 1999, *ApJ*, 521, 602
 ———. 2000, *ApJ*, 541, 734
 Binney, J. J., & Evans, N. W. 2001, *MNRAS*, 327, L27
 Blum, R. 1995, *ApJ*, 444, L89
 Bond, I. A., et al. 2001, *MNRAS*, 327, 868
 Crots, A. P. 1992, *ApJ*, 399, L43
 Dwek, E., et al. 1995, *ApJ*, 445, 716
 Evans, N. W., & Belokurov, V. 2002, *ApJ*, 567, L119
 Gates, E., Gyuk, G., & Turner, M. S. 1996, *Phys. Rev. D*, 53, 4138
 Gondolo, P. 1999, *ApJ*, 510, L29
 Gould, A. 1996, *ApJ*, 470, 201
 Gould, A., & An, J. H. 2002, *ApJ*, 565, 1381
 Gould, A., Popowski, P., & Terndrup, D. M. 1998, *ApJ*, 492, 778
 Griest, K., & Safizadeh, N. 1998, *ApJ*, 500, 37
 Griest, K., et al. 1991, *ApJ*, 372, L79
 Gyuk, G., & Crots, A. 1999, preprint (astro-ph/9904314)
 Han, C. 1999, *MNRAS*, 309, 373
 ———. 2000, *MNRAS*, 312, 807
 Han, C., & Gould, A. 1995a, *ApJ*, 447, 53
 Han, C., & Gould, A. 1995b, *ApJ*, 449, 521
 ———. 1996, *ApJ*, 467, 540
 Holtzman, J. A. 1998, *AJ*, 115, 1946
 Kerins, E., et al. 2001, *MNRAS*, 323, 13
 Kiraga, M., & Paczyński, B. 1994, *ApJ*, 430, L101
 Mera, D., Chabrier, G., & Schaeffer, R. 1998, *A&A*, 330, 937
 Nakamura, T., & Nishi, R. 1998, *Prog. Theor. Phys.*, 99, 963
 Ng, Y. K., et al. 1996, *A&A*, 310, 771
 Paczyński, B. 1986, *ApJ*, 304, 1
 ———. 1991, *ApJ*, 371, L63
 Paczyński, B., et al. 1994, *ApJ*, 435, L113
 ———. 1999, *Acta Astron.*, 49, 319
 Peale, S. J. 1998, *ApJ*, 509, 177
 Phillips, A. C., & Davis, L. E. 1995, *ASP Conf. Ser. 77, Astronomical Data Analysis and Software System IV*, ed. R. A. Shaw et al. (San Francisco: ASP), 297
 Popowski, P. 2002, *MNRAS*, submitted (astro-ph/0205044)
 Popowski, P., et al. 2001, in *ASP Conf. Ser. 239, Microlensing 2000: A New Era of Microlensing Astrophysics*, ed. J. W. Menzies & P. D. Sackett (San Francisco: ASP), 244
 Scalo, J. M. 1986, *Fundam. Cosmic Phys.*, 11, 1
 Schechter, L., Mateo, M., & Saha, A. 1993, *PASP*, 105, 1342
 Stanek, K. Z. 1996, *ApJ*, 460, L37
 Sumi, T., & Honma, M. 2000, *ApJ*, 538, 657

Tomany, A. B., & Crotts, A. P. 1996, *AJ*, 112, 2872
Udalski, A., et al. 1994, *Acta Astron.*, 44, 165
———. 2000, *Acta Astron.*, 50, 1
Woźniak, P. R. 2000, *Acta Astron.*, 50, 421
Woźniak, P. R., & Stanek, K. Z. 1996, *ApJ*, 464, 233

Woźniak, P. R., et al. 2001, *Acta Astron.*, 51, 175
Yanagisawa, T. 2000, *Exp. Astron.*, 10, 519
Zhao, H., & Mao, S. 1996, *MNRAS*, 283, 1197
Zhao, H., Spiegel, D. N., & Rich, R. 1995, *ApJ*, 440, L13